Extremely low structural hydroxyl contents in upper mantle xenoliths from the Nógrád-Gömör Volcanic Field (northern Pannonian Basin): Geodynamic implications and the role of post-eruptive re-equilibration

Levente Patkó, Nóra Liptai, István János Kovács, László El Aradi, Qun-Ke Xia, Jannick Ingrin, Judith Mihály, Suzanne Y. O'Reilly, William L. Griffin, Viktor Wesztergom, et al.

Chemical Geology 507 (2019) 23–41

Contents lists available at ScienceDirect

Chemical Geology

journal homepage: www.elsevier.com/locate/chemgeo

Extremely low structural hydroxyl contents in upper mantle xenoliths from the Nógrád-Gömör Volcanic Field (northern Pannonian Basin): Geodynamic implications and the role of post-eruptive re-equilibration

Levente Patkó[a], Nóra Liptai[a,b,c], István János Kovács[c,*], László Előd Aradi[a], Qun-Ke Xia[d], Jannick Ingrin[e], Judith Mihály[f], Suzanne Y. O'Reilly[b], William L. Griffin[b], Viktor Wesztergom[c], Csaba Szabó[a]

[a] Lithosphere Fluid Research Lab, Institute of Geography and Earth Sciences, Eötvös University, Budapest, Hungary
[b] Australian Research Council Centre of Excellence for Core to Crust Fluid Systems (CCFS) and GEMOC, Department of Earth and Planetary Sciences, Macquarie University, Sydney, Australia
[c] MTA CSFK Lendület Pannon LitH_2Oscope Research Group, Geodetic and Geophysical Institute, Research Centre for Astronomy and Earth Sciences, Hungarian Academy of Sciences, Sopron, Hungary
[d] School of Earth Sciences, Zhejiang University, Hangzhou, China
[e] Univ. Lille, CNRS, INRA, ENSCL, UMR 8207, UMET, Unité Matériaux et Transformations, F 59 000 Lille, France
[f] Research Centre for Natural Sciences, Hungarian Academy of Sciences, Budapest, Hungary

ARTICLE INFO

Editor: D.B. Dingwall

Keywords:
Upper mantle xenoliths
Nominally anhydrous minerals
Structural hydroxyl
Mantle mineral re-equilibration
Lithosphere extension
Dry mantle metasomatism

ABSTRACT

The structural hydroxyl content of the nominally anhydrous minerals (olivine and pyroxenes) in the upper mantle is among the important attributes that influence the physical and chemical features of the upper mantle. In this study, we provide detailed Fourier-transform infrared (FTIR) data on 63 petrographically and geochemically well-defined upper mantle xenoliths from the Nógrád-Gömör Volcanic Field (Pannonian Basin, Central Europe). These xenoliths show extremely low average structural hydroxyl contents (~0, 31 and 185 ppm for olivine, orthopyroxene and clinopyroxene, respectively) compared to values reported regionally and worldwide. The studied xenoliths have anomalous types of FTIR spectra and high structural hydroxyl ratios between clinopyroxenes and orthopyroxenes (an average of ~8). Furthermore, there is usually no correlation between the structural hydroxyl content and other physical or chemical properties of the xenoliths. These specific FTIR characteristics suggest that the Nógrád-Gömör upper mantle xenoliths were exposed to significant modification of their structural hydroxyl contents, which may be linked to pre- and post-eruptive processes. Decompression during extension leads to lower 'water' activity, which is most likely to have played a key role. However, pre-eruptive mantle metasomatism with an agent having low water activity cannot be excluded either. The post-eruptive cooling can be significant as well, as suggested by the higher structural hydroxyl content in xenoliths hosted in more rapidly cooled volcanic facies (i.e. pyroclastics).

Our study reveals how FTIR characteristics may evolve in continental rift settings in young extensional basins. Furthermore, novel applications of our study are the diagnostic features that indicate significant changes in structural hydroxyl properties. This contributes to distinguishing low structural hydroxyl contents linked to the pre-eruptive (i.e., low structural hydroxyl content in pyroxenes, anomalous partitioning and anomalous band characteristic in pyroxenes) or the post-eruptive (completely 'dry' olivines) periods.

1. Introduction

Structural hydroxyl refers to hydrogen incorporated in the crystal lattice of nominally anhydrous minerals (NAMs). If other forms of hydrogen are discussed they will be referred to specifically. The structural hydroxyl content of the lithospheric mantle is crucial, as it is thought to play a key role in influencing the melting temperature (Green et al., 2010), rheological properties (Karato and Jung, 2003; Kohlstedt, 2006; Demouchy et al., 2012; Girard et al., 2013; Bollinger et al., 2014), electrical conductivity (Selway et al., 2014), seismic wave attenuation

* Corresponding author.
E-mail address: kovacs.istvan.janos@csfk.mta.hu (I.J. Kovács).

https://doi.org/10.1016/j.chemgeo.2018.12.017
Received 30 July 2018; Received in revised form 9 December 2018; Accepted 19 December 2018
Available online 03 January 2019

(Aizawa et al., 2008) and deformation patterns (Jung et al., 2006; Manthilake et al., 2013). Furthermore, since hydrogen is considered as a highly incompatible element (Hirschmann et al., 2009) the structural hydroxyl contents of mantle xenoliths can be associated with metasomatic processes as well. Thus, it is important to characterize the distribution of structural hydroxyl in the lithosphere and monitor its variation with respect to major- and trace-element geochemistry and deformation patterns.

In mantle environment, 'water' can occur either as molecular water in fluid inclusions and bubbles of silicate melt inclusions (e.g. Berkesi et al., 2009; Hidas et al., 2010) or as structurally bound hydroxyl incorporated in mineral structures (e.g. Bell and Rossman, 1992; Demouchy and Bolfan-Casanova, 2016; Peslier et al., 2017; Xia et al., 2017). Hydrous mantle phases such as amphibole and mica can contain appreciable structural hydroxyl (1.5–5 wt%), however, their modal presence is usually low (< 5 vol%). Furthermore, amphibole is only stable in conditions below ~1100 °C and ~3 GPa (Green et al., 2010; Mandler and Grove, 2016). Hence, despite their relatively low contents of structurally bound hydroxyl (tens to few hundred ppm), NAMs such as olivine, orthopyroxene and clinopyroxene, which compose most of the upper mantle, control the concentration and distribution of structural hydroxyl below the Moho (e.g. Bell and Rossman, 1992; Peslier, 2010; Peslier et al., 2017).

In this paper, we report an exceptionally large number of Fourier-transform infrared (FTIR) analyses of NAMs in 63 upper mantle xenoliths with variable compositions from the Nógrád-Gömör Volcanic Field (Pannonian Basin, Central Europe), providing one of the most detailed studies in this field so far. Spinel peridotite xenoliths of this locality, which are hosted by both effusive and pyroclastic alkali basalts, were thoroughly investigated both geochemically (major and trace element characteristics) and seismically (seismic anisotropy, SKS delay time) in previous studies (Patkó et al., 2013; Klébesz et al., 2015; Liptai et al., 2017). Consequently, a detailed comparison of the structurally bound hydroxyl contents with different physical and geochemical parameters is possible. However, there are only a few papers concerning the question whether the structural hydroxyl contents in NAMs are representative of their original mantle environment or not (Denis et al., 2013, 2015, 2018; Lloyd et al., 2016; Tian et al., 2017)? In this paper, we assemble spectral features and physico-chemical characteristics, which unequivocally infer re-equilibration of structural hydroxyl during pre-, syn- or post-eruptive stages. Therefore, this detailed case study aims to provide guidelines for how re-equilibration of structural hydroxyl can be identified in upper-mantle xenoliths related to extensional geodynamic settings and post-eruptive processes.

2. Geological background

The Pannonian Basin is an extensional back-arc basin (Royden et al., 1982; Csontos et al., 1992; Horváth, 1993) situated in Central Europe, and is surrounded by the Alpine, Carpathian and Dinaric orogenic belts (Fig. 1a). The dominantly young (Neogene) sediment-covered basin (e.g. Magyar et al., 2013) consists of two different tectonic mega-units, which are the ALCAPA (ALps-CArphathian-PAnnonian block) in the northwest with Mediterranean affinity, and the Tisza-Dacia block in the southeast, of European origin (Balla, 1984; Csontos et al., 1992; Csontos and Vörös, 2004). The two microplates are separated by the Mid-Hungarian Shear zone (Csontos and Nagymarosy, 1998). The juxtaposition of the two mega-units started in the late Oligocene with the extrusion of ALCAPA from the Alpine collision zone due to the northward movement of the Adriatic microplate (Kázmér and Kovács, 1985; Ratschbacher et al., 1991; Horváth, 1993), and was further aided by an asthenospheric flow (Kovács et al., 2012a). The docking of the mega-units in the Carpathian embayment was followed by significant extension in the latest early Miocene (Bada and Horváth, 2001; Huismans et al., 2001). Several processes have been proposed as the main cause of the extension, such as subduction roll-back (Royden et al., 1982; Horváth, 1993), asthenospheric up-doming (Stegena et al., 1975), asthenospheric flow (Kovács et al., 2012a) coupled with thermal erosion, gravitational instability of the mantle lithosphere (Houseman and Gemmer, 2007), or various combinations of these effects.

The evolution of the basin was accompanied by widespread volcanic activity during the last 21 Ma, including the silicic, calc-alkaline and alkali volcanic magmatism (Szabó et al., 1992; Harangi, 2001; Kovács and Szabó, 2008; Lexa et al., 2010). The formation of monogenetic alkali mafic/basaltic volcanic fields took place during the last 10 Ma (Pécskay et al., 2006). Their generation is conventionally explained by adiabatic decompression melting in the upwelled and thermally relaxing asthenosphere in the post-extensional period (e.g. Embey-Isztin et al., 1993; Seghedi et al., 2004; Harangi et al., 2015). Alternatively, compression during the tectonic inversion of the region may have squeezed partial melt out from the asthenospheric dome, to be trapped between the converging Adriatic plate and the European platform. The ascent of basaltic melts to the surface may have been also facilitated by the formation of deep fractures in the folding lithosphere in the same compressional stress field (Kovács et al., 2018). The alkali basalts brought upper-mantle xenoliths to the surface in five occurrences scattered in the region, out of which the NGVF is the northernmost (Fig. 1a).

3. Sampling localities and sample description

The 63 xenoliths presented in this paper were the focus of previous geochemical and microstructural studies (Patkó et al., 2013; Liptai et al., 2017; Liptai et al., in prep). The xenoliths can be divided into wehrlite (Patkó et al., 2013) and lherzolite groups (Liptai et al., 2017; Liptai et al., in prep). The wehrlite series consists of 12 xenoliths, which are exclusively from the central part of the NGVF (Fig. 1b). The lherzolite series consists of 51 xenoliths, which, in addition to central-part localities, also occur in the northern and southern segments of the NGVF (Fig. 1b). These cover all the known xenolith-bearing localities in NGVF. With the exception of Jelšovec, where xenoliths occur in pyroclastic rocks, all xenoliths are hosted in lavas (Fig. 1b).

The studied xenoliths are angular or rounded and relatively small (3–5 cm in diameter), and careful selection preceded the analyses in order to avoid basalt infiltration. Xenoliths with surface alteration (e.g. iddingsite) were omitted from further investigation.

4. Analytical method and data processing

FTIR microscopic analysis to analyze structural hydroxyl in NAMs was performed in the Research Centre for Natural Sciences of the Hungarian Academy of Sciences in Budapest using a Varian FTS 7000 FTIR spectrometer coupled to a Varian UMA-600 IR microscope, and at the Geochemical Analysis Unit at Macquarie University in Sydney, applying a ThermoFisher iN10 FTIR microscope attached to a Varian FTS-60A spectrometer. The analyses were performed using unpolarized infrared light. Infrared spectra of olivine and pyroxenes were obtained between 4000 and 400 cm^{-1}, using a maximum of 100 × 100 μm aperture size. The samples were measured with a 'Globar' light source, KBr beam-splitter and an MCT detector. At least 128 scans were accumulated from each spot with a 4 cm^{-1} resolution. During the measurements the sample chamber and the interferometer were constantly flushed with compressed nitrogen to reduce background related to atmospheric moisture and carbon dioxide.

The method of Kovács et al. (2008) and Sambridge et al. (2008) for unpolarized infrared light makes it possible to determine the concentration of structural hydroxyl accurately even from few ($n > 5$) unoriented anisotropic crystals such as olivine and pyroxenes. Obviously the more unoriented grains are considered, the more accurate is the estimation. However, the accuracy of pyroxene measurements can be still satisfactory if < 5 or even only one unoriented grains are considered (Xia et al., 2013a; Liu et al., 2015). This method may be applied

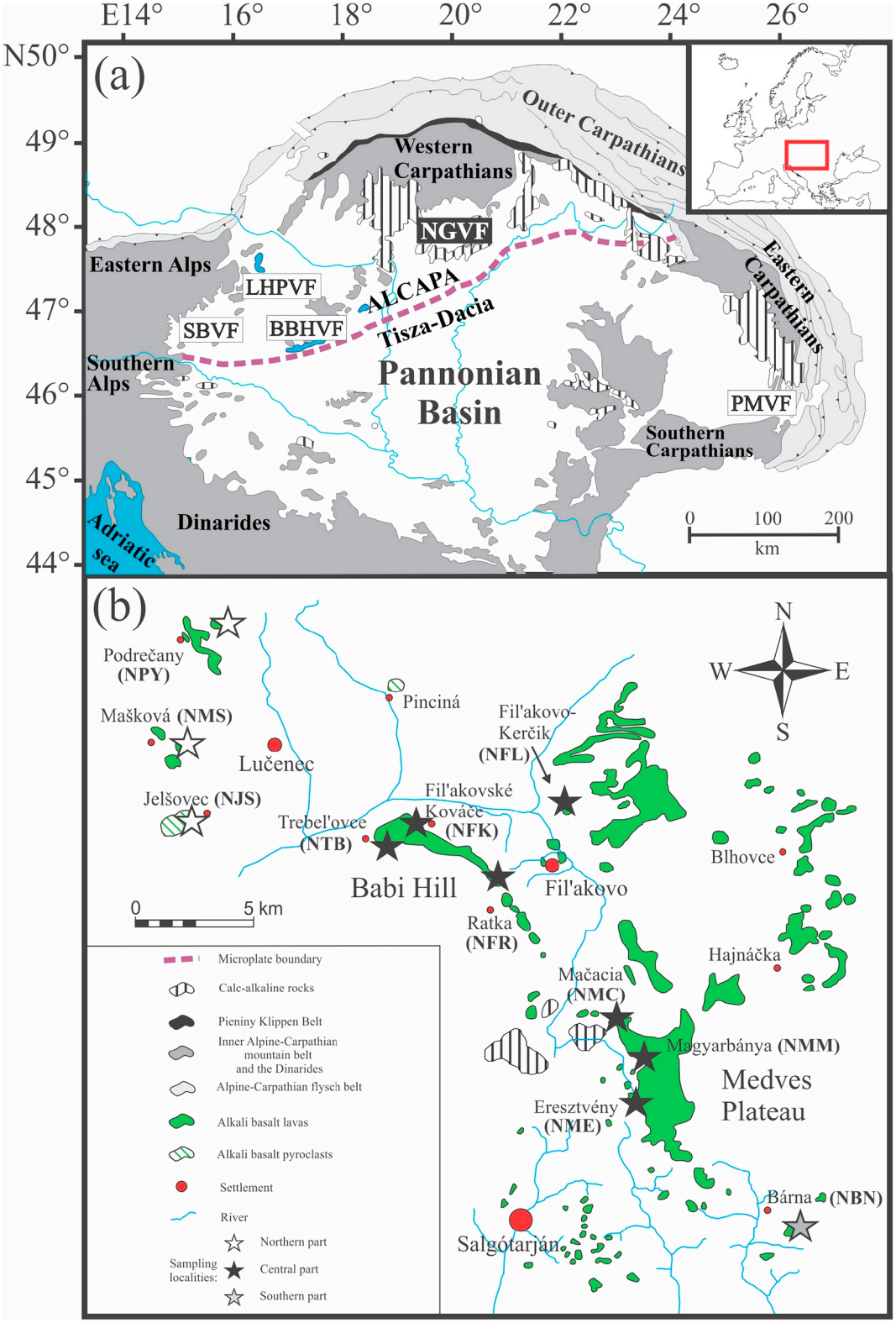

Fig. 1. (a) Simplified geological map of the Carpathian-Pannonian region with the assumed ALCAPA - Tisza-Dacia microplate boundary (after Csontos and Nagymarosy, 1998 and references therein). Xenolith-bearing Neogene alkali basalt occurrences are depicted using abbreviations: SBVF, Styrian Basin Volcanic Field; LHPVF, Little Hungarian Plain Volcanic Field; BBHVF, Bakony–Balaton Highland Volcanic Field; NGVF, Nógrád–Gömör Volcanic Field; PMVF, Perşani Mountains Volcanic Field. (b) Alkali basalt occurrences and xenolith sampling locations in the Nógrád-Gömör Volcanic Field (modified after Jugovics, 1971); quarries or outcrops from NW to SE can be divided into three parts. Namely these are the following: northern segment: Podrečany (NPY), Mašková (NMS), Jelšovec (NJS); central segment: Fil'akovo-Kerčik (NFL), Trebel'ovce (NTB), Fil'akovské Kováče (NFK), Ratka (NFR), Mačacia (NMC), Magyarbánya (NMM) Eresztvény (NME) and southern segment: Bárna (NBN).

Table 1
FTIR characteristics and structural hydroxyl contents (expressed in H_2O equivalent in ppm wt%) of the studied xenoliths.

Sample	Olivine			Orthopyroxene				Clinopyroxene					Bulk rock[0]
	Absorption bands	Analyzed grains	H_2O (ppm)	Absorption bands	Analyzed grains	Spectrum type	H_2O (ppm)	Absorption bands	Analyzed grains	Spectrum type	H_2O (ppm)	$D^{cpx/opx}$	H_2O (ppm)
Lherzolite series													
NMS1302A	–	–	–	3600, 3419	6	2a	3.29	3676[b], 3637, 3527, 3443, 3220[a]	4	1	140[d]	42.6	7.2
NMS1304	–	–	–	3598, 3412	4	2a	15.2	3636	5	1	18.7	1.2	2.9
NMS1305	–	–	–	3598, 3523[a], 3420	7	2a	2.89	3630, 3521[a]	6	1	112[c]	38.9	10.8
NMS1308	–	–	–	3598, 3522, 3420	5	2a	6.75	3629, 3524, 3442[a]	3	1	48.1	7.1	5.7
NMS1310	–	–	–	3588, 3568, 3522, 3421	4	2b	11.1	3630, 3522, 3445[a]	5	1	66.5	6.0	12.4
NJS1302	3572, 3525	10	2.82	3595, 3523, 3420	7	1	46.5	3628, 3526[a], 3449[a]	6	1	166	3.6	26.8
NJS1304	3572, 3525	8	4.18	3585, 3522, 3420	6	1	72.9[e]	3600, 3525[a], 3455, 3250	4	1	327	4.5	28.4
NJS1306	3568, 3525	11	3.29	3592, 3522, 3422	6	1	90.6	3627, 3528, 3455	5	1	342	3.8	72.0
NJS1307	3572, 3525	11	2.88	3592, 3523, 3420	6	1	98.2	3629, 3528, 3455	6	1	282	2.9	52.5
NPY1301	–	–	–	3598	6	1	–	3616	6	1	33.7	–	2.0
NPY1310	–	–	–	–	3	–	–	3620	4	1	–	–	–
NPY1311	–	–	–	3588, 3567	7	1	–	3609	6	1	–	–	–
NPY1314	–	–	–	3597	5	2a	–	3624, 3514	5	2b	19.2	–	3.5
NFL1302	–	–	–	3586, 3566, 3522, 3420	5	1	33.0[e]	3629, 3525, 3450	4	2a	149	4.5	15.2
NFL1305	–	–	–	3695[b], 3595, 3521, 3422	4	2a	95.2[d]	3697[b], 3628, 3538, 3452	4	2a	360[d]	3.8	70.8
NFL1315A	–	–	–	3595, 3505[a]	7	2a	–	3630, 3524, 3445	2	2b	57.5[e]	–	1.2
NFL1316	–	–	–	3596, 3521, 3418	6	1	9.34	3633, 3528[a], 3450[a]	2	1	122	13.0	7.0
NFL1324	–	–	–	3588, 3568, 3520	5	2b	16.3	3633, 3524[a]	4	1	81.9[e]	5.0	10.6
NFL1326	–	–	–	–	–	–	–	3630, 3525, 3440[a]	7	2a	86.4	–	10.4
NFL1327	–	–	–	–	–	–	–	3630, 3536, 3452	6	1	265	–	26.5
NFL1329	–	–	–	3595, 3521, 3421, 3200[a]	6	1	30.1	3628, 3525, 3446[a]	6	2a	122	4.0	17.5
NTB0306	–	–	–	3681[b], 3598, 3425	4	2a	62.3[d]	3632, 3539, 3453	8	1	121	1.9	19.3
NTB0307	–	–	–	3693[b], 3625, 3597, 3425, 3228[a]	6	2a	92.6[d]	3692[b], 3629, 3547, 3442[a], 3233[a]	3	1	388[d]	4.2	64.8
NTB1124	–	–	–	3585, 3566, 3521, 3416	15	2b	23.2	3629, 3521, 3461[a]	11	2b	126	5.4	20.7
NTB1116	–	–	–	3594, 3521, 3422	7	1	29.6[c]	3629, 3524, 3448[a]	7	2a	163	5.5	22.5
NTB1122	–	–	–	3593, 3521, 3426	6	2a	32.2	3628, 3523, 3450[a]	6	2b	188	5.8	34.3
NFK0301	–	–	–	3592, 3520, 3425	4	1	27.1	3628, 3528, 3440	5	1	265	9.8	19.5
NFK1123	–	–	–	3595, 3521, 3421	9	2a	73.5	3629, 3544, 3447	4	1	299	4.1	39.2
NFK1108	–	–	–	3590, 3523, 3420	7	1	14.8	3628, 3525, 3450[a]	7	2a	80.8	5.5	5.7
NFK1115	–	–	–	3599, 3420	7	2a	4.30	3689[b], 3633, 3527, 3442	7	1	88.7[d]	20.6	3.9
NFR0306	–	–	–	–	–	–	–	3627, 3527, 3450[a]	6	1	258	–	23.3
NFR0307	–	–	–	3681[b], 3634[a], 3600, 3427, 3250[a]	3	2a	147[d]	3681[b], 3632, 3441[a]	5	1	481[d]	3.3	59.8
NFR1109	–	–	–	3597, 3438	10	2a	8.76	3673[b], 3628, 3525, 3448	5	1	145[d]	16.6	8.7
NFR0309	–	–	–	3594, 3523, 3420, 3268[a]	7	2a	44.0	3628, 3525, 3450[a]	6	1	236	5.4	36.7
NFR1107	–	–	–	3596, 3522[a], 3420	5	2a	9.76	3669[b], 3629, 3525, 3450[a]	6	1	96.7[d]	9.9	8.5
NMC1301	–	–	–	3599, 3423	7	2a	5.27	3630, 3528, 3450	6	1	41.9	7.9	2.7
NMC1309	–	–	–	3598, 3423[a]	6	2a	6.74[c]	3629, 3524	5	2b	42.2	6.3	6.3
NMC1322	–	–	–	3595, 3420[a]	7	1	1.08	3620	6	1	19.5	18.0	1.7
NMC1336A	–	–	–	3595, 3420[a]	6	2a	1.49	3628, 3525, 3444, 3250	6	1	10.7	7.2	1.2
NMM1126	–	–	–	3587, 3566, 3521, 3405[a]	3	2b	24.9	3628, 3521	5	2b	36.9	1.5	11.2
NMM0318	–	–	–	3586, 3567, 3522	12	2b	3.94	3628, 3518	7	1	0.54	0.1	0.9
NMM1115	–	–	–	3567, 3522, 3414	4	2b	14.5	3628, 3522, 3450[a]	3	2b	67.3	4.6	5.5
NME1122	–	–	–	3585, 3566, 3521	2	2b	7.75	3628, 3522, 3447[a]	5	2a	63.2	8.2	7.8
NME0528	–	–	–	–	2	2b	–	3631, 3522	3	2b	38.0	–	2.3
NME1116	–	–	–	3587, 3567, 3524	6	1	–	3616, 3524	6	2b	48.0	–	5.3
NBN0302A	–	–	–	3586, 3566, 3522, 3420[a]	24	1	9.20	3672[b], 3628, 3528	5	1	42.5[d]	4.6	3.3
NBN0305	–	–	–	3598, 3420	10	2a	10.0	3684[b], 3637, 3560, 3450	5	1	45.9[d]	4.6	4.2

(*continued on next page*)

Table 1 (*continued*)

Sample	Olivine			Orthopyroxene				Clinopyroxene				Bulk rock[0]	
	Absorption bands	Analyzed grains	H_2O (ppm)	Absorption bands	Analyzed grains	Spectrum type	H_2O (ppm)	Absorption bands	Analyzed grains	Spectrum type	H_2O (ppm)	$D^{cpx/opx}$	H_2O (ppm)
NBN0311	–	–	–	3675[b], 3596, 3422, 3250[a]	8	2a	31.0[d]	3670[b], 3628, 3525, 3450[a]	4	1	71.2[d]	2.3	9.6
NBN0316	–	–	–	3596, 3425	17	2a	10.3	3674[b], 3637, 3525, 3450[a]	9	1	71.1[d]	6.9	7.3
NBN0319	–	–	–	3597, 3426	11	2a	12.7	3635, 3522, 3450[a]	10	2b	94.3	7.4	13.9
NBN0321	–	–	–	3596, 3522[a], 3422	11	2a	12.6	3628, 3526	9	1	87.8	7.0	10.4

Sample	Inhomogeneity groups	Olivine			Orthopyroxene				Clinopyroxene				Bulk rock[f]	
		Absorption bands	Analyzed grains	H_2O (ppm)	Absorption bands	Analyzed grains	Spectrum type	H_2O (ppm)	Absorption bands	Analyzed grains	Spectrum type	H_2O (ppm)	$D^{cpx/opx}$	H_2O (ppm)
Wehrlite series														
NTB1109	Dry	–	–	–	–	–	–	–	3689[b], 3629, 3524, 3450[a]	9	1	227[c]	–	43.0
	Wet	–	–	–	–	–	–	–	3691[b], 3628, 3527, 3446[a], 3251[a]	3	1	836[d]	–	
NTB1120	Dry	–	–	–	–	–	–	–	3693[b], 3631, 3444[a]	3	1	464[c]	–	111.4
	Wet	–	–	–	–	–	–	–	3687[b], 3630, 3526[a], 3447[a], 3245[a]	2	1	894[d]	–	
NFK1110	Dry	–	–	–	–	–	–	–	3687[b], 3630, 3524, 3450[a]	14	2a	131[c]	–	26.9
	Wet	–	–	–	–	–	–	–	3688[b], 3628, 3526, 3447[a]	2	1	363[d]	–	
NFK1137A	Dry	–	–	–	–	–	–	–	3689[b], 3633, 3525, 3451[a]	3	1	109[d]	–	25.0
	Wet	–	–	–	–	–	–	–	3694[b], 3631, 3529, 3453[a]	7	1	360[d]	–	
NFR1117A	Dry	–	–	–	–	–	–	–	3630, 3525	11	1	202[c]	–	42.5
	Wet	–	–	–	–	–	–	–	3675[b], 3628, 3401[a], 3249[a]	1	1	518[d]	–	
NFR1119B	Dry	–	–	–	–	–	–	–	3631, 3525	4	1	20.5	–	2.1
	Wet	–	–	–	–	–	–	–	3631	5	1	550[d]	–	
NMC1302B	Dry	–	–	–	–	–	–	–	3629, 3521[a]	8	1	46.7[c]	–	10.4
	Wet	–	–	–	–	–	–	–	3693[b], 3630	1	1	269[d]	–	
NMC1343	Dry	–	–	–	–	–	–	–	3629, 3526	8	2a	53[c]	–	10.6
	Wet	–	–	–	–	–	–	–	3627, 3523	1	2b	294[d]	–	
NMM1114	Dry	–	–	–	–	–	–	–	3530, 3522	3	2b	59.5	–	14.0
	Wet	–	–	–	–	–	–	–	3628, 3522	5	2b	202[d]	–	
NMM1129	Dry	–	–	–	–	–	–	–	3630, 3526	4	1	82.3	–	14.5
NME1110	Dry	–	–	–	–	–	–	–	3629, 3528, 3451[a]	5	1	206[e]	–	45.6
	Wet	–	–	–	–	–	–	–	3687[b], 3629, 3528	7	1	431[d]	–	
NME1129D	Dry	–	–	–	–	–	–	–	3678[b], 3631, 3527	3	1	75.0[d]	–	17.3
	Wet	–	–	–	–	–	–	–	3683[b], 3633, 3427, 3248	10	1	573[d]	–	

[a] Weak band.
[b] Hydrous lamella.
[c] Inhomogeneous structural hydroxyl contents within the sample.
[d] Slightly overestimated results.
[e] Similar orientation in most of the grains.
[f] Based on the structural hydroxyl of NAMs.

only if the maximum linear unpolarized absorbance is < 0.15, a criterion that was always met in this study. The total polarized absorbance (A_{tot}) is estimated as three times the average unpolarized integrated absorbance. The A_{tot} for each NAM in each sample was obtained using the OPUS® software, applying the following steps: (1) background correction using the concave rubber-band correction routine with 2 iterations and 64 baseline points; (2) averaging the spectra; (3) integration of spectral ranges of structurally bound hydroxyl with B-type integration applying uniform intervals for each mineral (3583–3505 and 3290–3170 cm^{-1} for olivines; 3740–3020 cm^{-1} for orthopyroxenes and 3765–3000 cm^{-1} for clinopyroxenes). Integrated total absorbance values are normalized to 1 cm thickness. The thickness of the sections was measured with a Mitutoyo analogue micrometer, which is accurate to 2–3 μm within the thickness range considered. The A_{tot} is then converted to absolute concentration of structural hydroxyl (expresses as H_2O equivalent in ppm wt%) using the mineral-specific calibration factors of Bell et al. (1995) for ortho- ($k_{opx} = 0.0674$) and clinopyroxene ($k_{cpx} = 0.14$) and $k_{ol} = 0.188$ for olivine (Bell et al., 2003). In the case of olivine, calculations of structural hydroxyl content using site specific absorption coefficients were also carried out ($k_{ol[Ti]} = 0.18$ and $k_{ol[Mg]} = 0.03$; Kovács et al., 2010). Since the calculations using the different factors led to similar results, we only used values gained by the mineral specific calibration of Bell et al. (2003) in this study because of its more frequent application in the literature. It was recently argued that the wavenumber-dependent calibration by Libowitzky and Rossman (1997) is more suitable for diopside (Weiss et al., 2018). However, for the sake of comparing our results with previous ones, we preferred to keep the same calibration that is generally used for pyroxenes. Note that the calibration factor is often used equally as integral molar extinction (or absorption) coefficient (ε [$L / mol * cm^2$)) which is related to the k calibration factor through the following formula: $k = M_A / (\rho * \varepsilon)$, where the M_A is the molar weight of water (18.02 g), ρ is density of the target mineral in g/L.

The detection limit of the micro-FTIR technique for nominally anhydrous silicate minerals is routinely at or below 1 ppm for structural hydroxyl (e.g. Bell et al., 1995) if the measurement conditions are optimal. This means that the degree of atmospheric interference (e.g., atmospheric moisture and carbon-dioxide) is minimalized, the measurement spot is free of hydrous inclusions, contaminations and alteration products, the thin section is 200–300 μm thick and the aperture size is at least ~50 * 50 μm. This practice ensures the maximum signal to noise ratio during analysis.

Considering the uncertainties in the integral molar extinction coefficient (ε [$L / mol * cm^2$)]), density (ρ [g/L]), sample thickness (t [cm]) and total polarized absorbance (A_{tot} [cm^{-1}]) – assumed to be estimated based on five random measurements on unoriented grains with unpolarized radiation – the one σ relative uncertainties for structural hydroxyl content in olivine, orthopyroxene and clinopyroxene are 20, 7 and 6% respectively based on the error propagation formula in Table 5 of Liu et al. (2006). The uncertainties for ε and ρ are from Bell et al. (1995, 2003) and for the thickness measurement we assumed 1.5% relative uncertainty. The uncertainty in the estimation of the total polarized absorbance from the average of five random unoriented, unpolarized measurements was determined by a Monte Carlo simulation using the principal polarized absorbances of GRR1695-2 olivine (Bell et al., 2003), PMR-53 clinopyroxene and KBH-1 orthopyroxene (Bell et al., 1995) and Eq. (6) in Kovács et al. (2008) (see also Supplementary Table 1 for technical details). Note that the spectral characteristics of the applied mineral standard are usually more or less similar to the ones we observed. This cumulated uncertainty, nevertheless, is lower if the number of analyzed unoriented grains exceeds five, which is generally the case in our study, thus, these values represent only a worst case scenario.

5. Sample petrography and geochemistry

The NGVF upper mantle xenoliths, all spinel peridotites, show great variability both in petrography and geochemistry, which implies a heterogeneous mantle beneath the region (Liptai et al., 2017).

The wehrlite series is quite uniform in modal composition (72–82 vol% for olivine and 10–24 vol% for clinopyroxene) with only a few orthopyroxene remnants (< 1 vol%) enclosed in clinopyroxene and olivine. In two wehrlite xenoliths (NFK1137A, NMM1129) orthopyroxene is completely absent. Xenoliths of the lherzolite series, although they have great modal variability (43–89 vol% olivine, 1–46 vol% orthopyroxene and 2–19 vol% clinopyroxene), are dominantly lherzolites with minor wehrlites (NFL1326, NFL1327, NFR0306) and harzburgites (NFL1315A) (Table 1 in Liptai et al., 2017). These individual wehrlite specimens are distinguished from those in the wehrlite series by their petrographic and geochemical characteristics, having deformed grains in textural equilibrium and lower contents of basaltic major elements (Fe, Ti, Mn, Ca). The determined xenolith textural types are different for the two distinct series. Xenoliths of the lherzolitic series have porphyroclastic, protogranular and equigranular textures in decreasing order of frequency (Liptai et al., 2017). In contrast, the wehrlites show reaction textures with non-equilibrated replacement patterns and interlacing finger microtextures (Patkó et al., 2013).

The major and trace element geochemistry of wehrlites shows significant heterogeneity not only among xenoliths, but even within grains, which is not characteristic for xenoliths of the lherzolite group. The wehrlites are enriched in Fe, Mn, and Ca in olivine, Fe, Ti, Mn, and Ca in orthopyroxene, Fe, Ti, Al, Mn and light rare earth elements (LREE) in clinopyroxene and Fe and Ti in spinel compared to those in lherzolites. Xenoliths of the lherzolite series show wide variability in both major- and trace-element contents, as a result of heterogeneous partial melting and subsequent metasomatism. Some lherzolites have geochemical characteristics similar to the wehrlites, indicating a common mafic melt-related metasomatism (Liptai et al., 2017).

6. Infrared spectroscopy of nominally anhydrous minerals

Representative infrared spectra of NAMs from the examined Nógrád-Gömör xenoliths are depicted in Fig. 2. The estimated concentrations of structural hydroxyl are listed in Table 1. The structural hydroxyl content is mostly homogenous within single xenoliths belonging to the lherzolite series. However, rarely in the lherzolite series (e.g. NMS1305), but more frequently in the wehrlite series (e.g. NTB1120, NFR1117A) there are xenoliths which have heterogeneous structural hydroxyl contents not only within xenoliths, but even within individual mineral constituents.

6.1. Olivine

The thickness of olivine crystals analyzed ranged from 70 μm to 350 μm. With the exception of the four pyroclastite-hosted Jelšovec xenoliths (NJS), in which weak bands appear at ~3572, ~3525 and 3230 cm^{-1} (Fig. 2a, thicknesses 170 to 225 μm), there are no bands related to structural hydroxyl visible in olivine. The most intense linear absorption is always related to the ~3572 cm^{-1} band, which deviates a little in NJS1306, shifting towards a lower wavenumber (~3568 cm^{-1}). The band at ~3230 cm^{-1} is broad with a half width of ~40 cm^{-1} (Fig. 2a). The calculated structural hydroxyl content (expressed in H_2O equivalent in ppm wt%) exceeds 4 ppm only in one xenolith (NJS1304), whereas in the rest of the xenoliths (NJS1302, NJS1306, NJS1307) it is between 2.5 and 3.5 ppm (Table 1).

6.2. Orthopyroxene

The averaged unpolarized orthopyroxene FTIR spectra vary considerably, hence a classification was carried out based on the linear

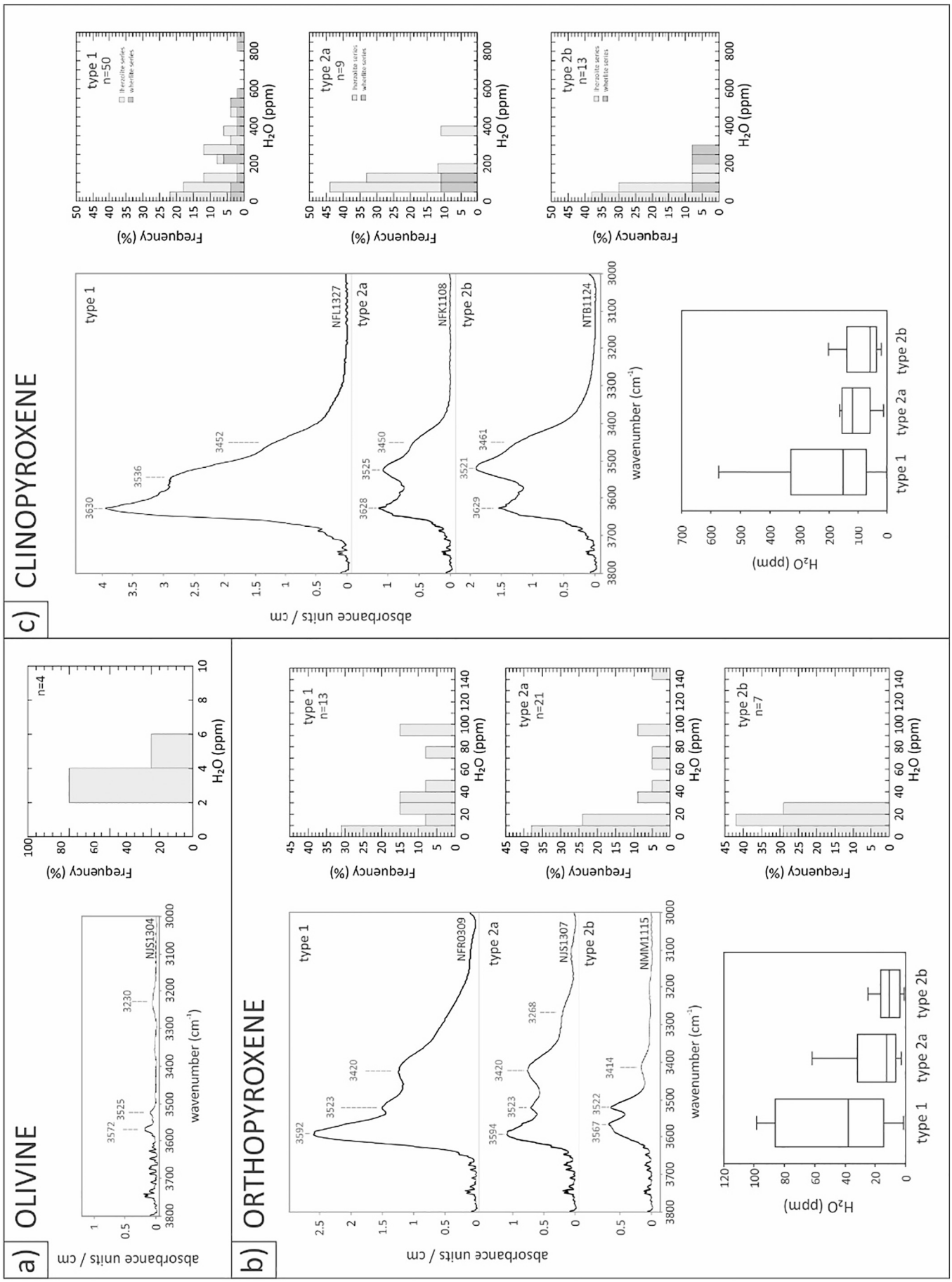
a) OLIVINE
absorbance units / cm
wavenumber (cm-1)
3572
3525
3230
NJS1304
Frequency (%)
n=4
H2O (ppm)
b) ORTHOPYROXENE
absorbance units / cm
wavenumber (cm-1)
type 1
3592
3523
3420
NFR0309
type 2a
3594
3523
3420
3268
NJS1307
type 2b
3567
3522
3414
NMM1115
type 1
n=13
type 2a
n=21
type 2b
n=7
Frequency (%)
H2O (ppm)
type 1
type 2a
type 2b
c) CLINOPYROXENE
absorbance units / cm
wavenumber (cm-1)
type 1
3630
3536
3452
NFL1327
type 2a
3628
3525
3450
NFK1108
type 2b
3629
3521
3461
NTB1124
type 1
n=50
type 2a
n=9
type 2b
n=13
hercynite series
wharfite series
Frequency (%)
H2O (ppm)
H2O (ppm)
type 1
type 2a
type 2b

Fig. 2. Representative average unpolarized spectrum types of (a) olivine, (b) orthopyroxene, and (c) clinopyroxene of the studied Nógrád-Gömör upper mantle xenoliths with accompanying histograms and box and whisker diagrams of the structural hydroxyl contents (expressed in H_2O equivalent in ppm wt%). The box and whisker diagram is a visualized five-number summary of a data set including minimum and maximum values, first and third quartile and the median.

absorption intensities and band positions (Fig. 2b). In some xenoliths of the lherzolite series, orthopyroxene analyses could not be carried out (Table 1), either because of the lack of orthopyroxene (NFL1326) or their insufficient size (NFL1327, NFR0306). Furthermore, in a few lherzolite xenoliths (NPY1301, NPY1310, NPY1311, NPY1314, NFL1315A, NME0528, NME1116) structural hydroxyl content was below the limit of detection. No appropriate orthopyroxene spectra were obtained from xenoliths of the wehrlite series either, because of the absence of orthopyroxene or the small size (200–400 μm) of orthopyroxene grains.

The three most intense bands are situated at ~3600, ~3525 and ~3420 cm^{-1} wavenumbers. However, less frequently appearing bands at ~3585 and 3565 cm^{-1} were also taken into account during classification. In xenoliths where any of these five bands were absent, absorption intensity values at the band positions were still read and used.

The band at ~3600 cm^{-1} is normally the most intense and absorption intensities decrease with decreasing wavenumber. This spectrum type is defined as type 1 (35% of all orthopyroxenes) (Fig. 2b). Spectrum types diverging from spectrum type 1 are referred as type 2, which have two subtypes. In the dominant 2a subtype, the spectrum is characterized by more intense absorption at ~3420 cm^{-1} compared to ~3525 cm^{-1} (50% of all orthopyroxenes) (Fig. 2b). In the less abundant type 2b orthopyroxene spectra (15% of all orthopyroxenes), a well-defined band appears at ~3565 cm^{-1}, always accompanied by a subtle shoulder at ~3585 cm^{-1} (or the other way around) (Fig. 2b). Usually, the former is more intense (NFL1324, NMM1115, NMM1126, NMM0318, NME1122), but in two xenoliths (NMS1310, NTB1124) the latter shows higher absorption intensity.

Besides these main absorption bands, there are less frequent bands occurring at ~3695–3675 cm^{-1} (Supplementary Fig. 1a) and ~3270–3200 cm^{-1} (Table 1; see spectra on PULI spectral database at puli.mfgi.hu). Bands in the former range are normally well-defined narrow bands (their half width ~10–20 cm^{-1}). In contrast, bands at lower wavenumbers are broader and weaker and only minimally contribute to the hydroxyl signal of the orthopyroxenes.

The structural hydroxyl contents in orthopyroxenes are extremely variable, ranging between 1 and 147 ppm (with an average of 31 ppm) (Table 1). In all three types, most orthopyroxenes have structural hydroxyl contents lower than 30 ppm (54, 62 and 100% of type 1, 2a and 2b, respectively) (Fig. 2b).

6.3. Clinopyroxene

Clinopyroxenes in all but two lherzolite xenoliths (NPY1310, NPY1311) contain measurable amounts of structural hydroxyl (Table 1). Clinopyroxene spectra are classified into three types based on the relative absorption intensities of the two most intense bands at ~3630 and ~3525 cm^{-1} (Table 1). Bands at the former position are always present, whereas bands at the latter one are occasionally absent. The three clinopyroxene types (1, 2a and 2b) are defined with quotients of the absorption intensity values of ~3630 and ~3525 cm^{-1} wavenumbers being > 1.2 (3630 cm^{-1} dominates), 1.0–1.2 (the two main bands are similar in intensity) and < 1.0 (3525 cm^{-1} band dominates), respectively (Fig. 2c). In most xenoliths, clinopyroxenes belong to type 1 (69%), whereas type 2a and 2b are present in 14 and 17%, respectively (Table 1).

In addition to the two main bands, several further bands appear in some of the clinopyroxene spectra (see spectra on PULI spectral database at puli.mfgi.hu). In several samples, spectra have shoulders at high wavenumbers (3695–3670 cm^{-1}) as in the orthopyroxenes (Supplementary Fig. 1b; Table 1). However, there are only a few lherzolite xenoliths (NTB0307, NFR0307, NFL1305, NBN0311) where these shoulders appear simultaneously in both pyroxenes. Further weak bands are sometimes present at ~3455–3445 and ~3250–3230 cm^{-1} (Table 1; see spectra on PULI spectral database at puli.mfgi.hu).

Xenoliths with type 1 clinopyroxenes have higher maximum and average contents of structural hydroxyl (0.5–894 ppm with an average of 217 ppm) than xenoliths with type 2a and type 2b clinopyroxenes (53–360 and 19–294 ppm with an average of 134 and 98 ppm, respectively) (Fig. 2c). Note that among type 2a clinopyroxenes the content of structural hydroxyl is always > 50 ppm. In contrast, the most dominant range of structural hydroxyl concentrations for clinopyroxenes with type 2b spectra is < 50 ppm (38%; Fig. 2c). Clinopyroxenes in the lherzolite series have structural hydroxyl concentrations of 0.5–481 ppm (with an average of 132 ppm) (Table 1). This variability is present in the wehrlite series as well. In addition, wehrlite xenoliths sometimes contain grains that are both poor (21–464 ppm) and rich in structural hydroxyl (202–894 ppm) with an average of 140 and 481 ppm structural hydroxyl, respectively (Table 1). Both types appear within individual xenoliths. Similarly, according to their petrographic and geochemical characteristics, the wehrlite xenoliths can be divided into two groups, one with less stealth metasomatism (lower basaltic major element and clinopyroxene enrichment) and one with extensively stealth metasomatism (higher basaltic major element and clinopyroxene enrichment) (Patkó et al., 2013). The only exception is wehrlite xenolith NMM1129, which contains only clinopyroxene poor in structural hydroxyl. Among the wehrlite xenoliths, all clinopyroxene spectrum types are present, with type 1 being the most dominant.

Type 1 clinopyroxene spectra are usually accompanied by 1 and 2a type orthopyroxene spectra (24 and 37%, respectively). Although all possible combinations of spectrum types are present in the NGVF, in addition to 1-1 and 1-2a, only 2b-2a clinopyroxene-orthopyroxene pairs have a higher abundance than 10% (11%).

6.4. Whole-rock structural hydroxyl content

Whole-rock contents of structural hydroxyl were calculated from analyses of the mineral constituents weighted by their modal proportion (Table 1). The bulk contents of structural hydroxyl range between 1 and 72 ppm (with an average of 17 ppm) and 2 and 111 ppm (with an average of 30 ppm) for xenoliths of the lherzolite and wehrlite series, respectively. The highest averaged whole-rock structural hydroxyl content is shown by the Jelšovec xenoliths (NJS) (up to 45 ppm). In these estimations, the hydrous phases were not considered because of their restricted appearance (i.e., amphibole content > 1 vol% only in lherzolite xenolith NMS1304, NFL1324 and NFL1326; Liptai et al., 2017).

7. Discussion

7.1. Interpretation of the infrared spectra

It is widely accepted that different stretching bands of structural hydroxyl on the FTIR spectra represent different modes of structural hydroxyl incorporation into NAMs (e.g. Beran and Putnis, 1983). In the NAMs of the upper mantle, incorporation of structural hydroxyl in olivine has been the best explored so far, due to its dominant role in regulating the physical properties of the upper mantle. Among the NGVF xenoliths, only olivines in a few samples from a single locality (Jelšovec - NJS) show absorption bands, albeit rather weak. These bands are situated at ~3572, ~3525 and ~3230 cm^{-1} (Fig. 2a). The first two wavenumber values are typical for Ti-clinohumite point

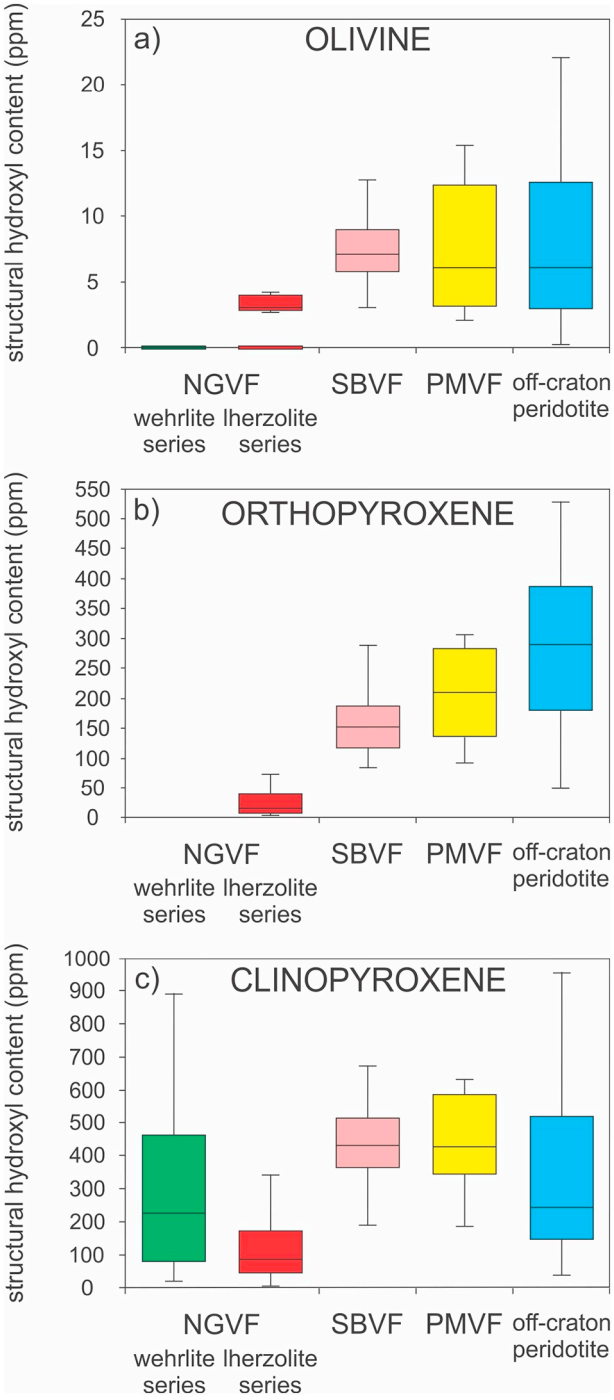

Fig. 3. Box and whisker diagram of the structural hydroxyl content (expressed in H_2O equivalent in ppm wt%) of (a) olivines (b) orthopyroxenes and (c) clinopyroxenes from CPR localities and worldwide off-craton peridotites. Box and whisker diagram is a visualized version of five-parameters including minimum and maximum values, first and third quartile and the median. Note that we distinguished the lherzolite and wehrlite series in case of Nógrád-Gömör data. Data sources are the following: Aradi et al., 2017 for SBVF xenoliths, Falus et al., 2008 for PMVF and Peslier, 2010 and references therein for the off-craton peridotites. Abbreviations: NGVF - Nógrád-Gömör Volcanic Field; SBVF - Styrian Basin Volcanic Field; PMVF - Perşani Mountains Volcanic Field.

defects [Ti], when a Ti^{4+} in the octahedral site is compensated by the incorporation of two hydrogens in the neighboring vacant tetrahedral site (e.g. Berry et al., 2005; Kovács et al., 2010). The band appearing at ~3230 cm^{-1} is linked to hydrogen incorporation into octahedral (Mg) vacancies [Mg] (e.g. Berry et al., 2005; Kovács et al., 2010). In many natural samples, the [Ti] substitution mechanism is the most common (e.g. Xia et al., 2010; Denis et al., 2015; Aradi et al., 2017), which agrees well with some laboratory experiments (e.g. Berry et al., 2005; Kovács et al., 2012b; Demouchy et al., 2017).

The three most intense stretching bands of structural hydroxyl in orthopyroxene are situated at ~3600, ~3525 and ~3420 cm^{-1} in the NGVF xenoliths (Fig. 2b). This agrees well with natural samples from several locations situated in a range of tectonic settings (Peslier et al., 2002; Bonadiman et al., 2009; Xia et al., 2010, 2013b; Yu et al., 2011; Demouchy et al., 2015; Denis et al., 2015; Li et al., 2015; Pintér et al., 2015; Hao et al., 2016a; Aradi et al., 2017). Most commonly, the dominant spectrum type is characterized by decreasing intensities of peaks from higher towards lower wavenumbers (type 1 in our nomenclature). In contrast, in the NGVF, only 35% of all orthopyroxene spectra belong to this group (Table 1). The spectrum type with a more intense band at ~3420 cm^{-1} than at ~3525 cm^{-1} (type 2a in our nomenclature), as well as spectra with intense bands at ~3565 cm^{-1} and ~3585 cm^{-1} (type 2b in our nomenclature) have both been described in the literature. However, their presence appears to be only subordinate (e.g. Demouchy et al., 2015; Gu et al., 2018). On the contrary, in the NGVF, type 2a and 2b orthopyroxenes occur frequently (50 and 15%, respectively; Table 1). Because of the more complex structure and presumably subordinate importance of orthopyroxene, and consequently the relatively limited research into this topic, it is currently ambiguous as to which substitution mechanisms of structural hydroxyl are related to specific bands. However, the available experimental results suggest that bands appearing at wavenumbers above 3400 cm^{-1} might be explained by coupled substitution mechanisms where structural hydroxyl is linked to trivalent cations in the orthopyroxene structure (Stalder and Skogby, 2002; Stalder, 2004). It is rather probable, however, that shoulder-like bands at ~3675–3695 cm^{-1} (Supplementary Fig. 1a) can be attributed to (often only nano-sized) hydrous lamellae in pyroxenes, most probably amphibole (Della Ventura et al., 2007; Kovács et al., 2012b). Note that this is not structural hydroxyl in the pyroxene structure, but the dissolution of separate hydrous minerals (e.g. amphibole or mica) from the pyroxene lattice itself.

Similarly to orthopyroxenes, the main bands in NGVF clinopyroxenes, located at ~3630 and ~3525 cm^{-1} (Fig. 2c), agree well with those reported in natural samples all over the world (Peslier et al., 2002; Bonadiman et al., 2009; Xia et al., 2010, 2013a, 2013b; Yu et al., 2011; Demouchy et al., 2015; Denis et al., 2015; Li et al., 2015; Pintér et al., 2015; Hao et al., 2016a; Aradi et al., 2017). In the most common (69%) spectrum type in the NGVF the peak at ~3630 cm^{-1} is more intense than the others (type 1 in our nomenclature). This observation is consistent with clinopyroxene spectra reported by other studies, irrespective of their tectonic setting (Bonadiman et al., 2009; Xia et al., 2013a; Pintér et al., 2015). Spectra with equal (type 2a in our nomenclature) or higher intensity (type 2b in our nomenclature) of the peak at 3525 relative to the one at ~3630 cm^{-1} (14 and 17% in the NGVF, respectively) have also been described from the North China Craton, albeit in significantly lower abundance (Xia et al., 2010, 2013b; Li et al., 2015). Akin to orthopyroxene, the incorporation mechanisms of structural hydroxyl in clinopyroxene are not yet fully understood. Nevertheless, the different bands are possibly linked to incorporation of coupled hydroxyl and trivalent cations or structural hydroxyls in vacant M- and Si-sites (Stalder and Ludwig, 2007). Bands at high wavenumbers (~3675–3695 cm^{-1}) (Supplementary Fig. 1b), as in orthopyroxene, can be ascribed to hydrous lamellae, most probably amphibole (Ingrin et al., 1989; Della Ventura et al., 2007). These related bands are more common in clinopyroxenes from the wehrlites than in those from the lherzolite series (Table 1.).

In conclusion, the spectral characteristics of olivines lack structural hydroxyl related bands with the exceptions of olivines from one locality (Jelšovec - NJS). Furthermore, in case of the orthopyroxenes and clinopyroxenes bands at lower wavenumbers (< 3600 cm^{-1} and < 3630 cm^{-1}, respectively) usually appear to play more important role than in

other pyroxenes worldwide, where the high wavenumber bands are the dominant ones.

7.2. Implications of the structural hydroxyl contents

The structural hydroxyl contents measured in olivine, orthopyroxene and clinopyroxene are given in Table 1. Most of the olivines are completely 'dry' (i.e. structural hydroxyl is below the limit of detection (≪1 ppm)). The few Jelšovec (NJS) xenoliths, which show weak bands related to structural hydroxyl (Fig. 2a), have only very low contents of structural hydroxyl (~2–4 ppm; Table 1). This observation is inconsistent with the generally higher structural hydroxyl contents reported from other localities in the Carpathian-Pannonian region (CPR) so far. Olivines in the Styrian Basin (SBVF) and Perşani Mountains (PMVF), located at the western and eastern edges of the CPR, respectively, have 3–13 ppm (with an average of ~7 ppm) (Aradi et al., 2017) and 2–15 ppm (with an average of ~6 ppm) (Falus et al., 2008) structural hydroxyl (Fig. 3a). This agrees well with olivine data from off-craton settings (Peslier, 2010; Demouchy and Bolfan-Casanova, 2016; Peslier et al., 2017; Fig. 3a). However, these low values are not unprecedented, as similarly 'dry' xenoliths have been reported from several locations in China (Yang et al., 2008; Bonadiman et al., 2009; Xia et al., 2010, 2013b; Hao et al., 2016a; Zhang et al., 2018), France (Gu et al., 2018) and USA (Denis et al., 2018).

Pyroxenes, however, do have detectable structural hydroxyl concentrations in almost all NGVF xenoliths (Table 1). The orthopyroxene and clinopyroxene values are between 1 and 147 ppm and 1–894 ppm, respectively (with averages of 31 and 165 ppm). Even though some pyroxenes include bands related to hydrous minerals at high wavenumbers (~3675–3695 cm^{-1}; Supplementary Fig. 1), the structural hydroxyl contents may be considered as robust, since these lamellae may have formed at the expense of structural hydroxyl in their host pyroxene (e.g. Kang et al., 2017; Schmädicke and Gose, 2017). Even if the source of excess hydroxyl for the formation of hydrous lamellae had been external, their spectral contribution would only cause a subtle overestimation (up to 5 ppm based on the integrated area of amphibole shoulder at 3695 cm^{-1} and the wavenumber specific calibration of Libowitzky and Rossman, 1997). All in all, the structural hydroxyl contents of the NGVF pyroxenes are lower than those in other xenolith-bearing localities in the CPR, which have an average of 156 and 433 ppm (values between 83 and 294 and 190–674 ppm, respectively for orthopyroxenes and clinopyroxenes) in the SBVF (Aradi et al., 2017) and an average of 206 and 447 ppm (for a range of 92–305 and 186–632 ppm) in the PMVF (Falus et al., 2008) (Fig. 3b–c). The SBVF and PMVF values overlap well with H_2O contents from off-cratonic xenoliths worldwide (Peslier, 2010; Demouchy and Bolfan-Casanova, 2016; Peslier et al., 2017; Fig. 3b–c), which suggests that the structural hydroxyl content of NGVF pyroxenes are low not only on a regional, but also on a global scale. Similarly 'dry' xenoliths have been described from a few localities in the North China Craton (Yang et al., 2008; Xia et al., 2010, 2013b).

Partition coefficients of structural hydroxyl between pyroxenes are highly variable (Fig. 4), ranging between 1 and 43 (Table 1). According to recent reviews (e.g. Demouchy et al., 2017; Peslier et al., 2017; Xia et al., 2017), $D^{cpx/opx}$ values for structural hydroxyl vary between 1.5 and 3.5 and this range can be considered as 'normal' for natural samples. Pyroxenes from the SBVF (Aradi et al., 2017) and the PMVF (Falus et al., 2008) usually fall within this range. Experimentally obtained $D^{cpx/opx}$ values are similar or slightly below this range (0.9–3.3) (Aubaud et al., 2004; Hauri et al., 2006; Tenner et al., 2009; Kovács et al., 2012b; Demouchy et al., 2017). In our study a great number of xenoliths have structural hydroxyl partition coefficients between pyroxenes higher than 3.5 (~ 80% of the NGVF xenoliths). A minor part of the NGVF xenoliths, which falls in the range defined by Xia et al. (2017), contains clinopyroxene-orthopyroxene pairs belonging to the 1-1 and 1-2a groups.

The bulk rock structural hydroxyl content of NGVF xenoliths averages 20 ppm (with a range of 1–111 ppm). These bulk rock data are lower than those in the SBVF (average of 452 ppm; Aradi et al., 2017) and the PMVF (average of 86 ppm; Falus et al., 2008). It should be noted that most of the SBVF xenoliths contain amphibole (up to 32 vol %), which significantly increases the bulk structural hydroxyl contents, but even considering this the bulk structural hydroxyl content of NGVF xenoliths is still relatively low.

In summary, structural hydroxyl contents of orthopyroxenes and clinopyroxenes in the NGVF xenoliths are low compared to those from other off-cratonic xenoliths worldwide. The partition coefficients of structural hydroxyl between pyroxenes in almost ~80% of the NGVF xenolith are higher (> 3.5) than other localities worldwide. This implies that this anomalously low structural hydroxyl content and high partition coefficient may have something to do with the geologically relatively young age of the extension (≪20 Ma) in the Pannonian Basin and the young alkaline basaltic volcanism (mostly between 7 and 2 Ma; Pécskay et al., 2006). Therefore the Pannonian Basin offers us an excellent natural laboratory where these geologically young ages and the short time elapsed between the extension and alkaline basaltic volcanic activity have the capacity to provide information on the possible effect of extension on the structural hydroxyl content of NAMs.

7.3. Relationship between geochemical and physical variables and the hydroxyl content

Hydrogen is a highly incompatible element ($D^{peridotite/melt}$ (H_2O) ~ 0.001–0.01; Hirschmann et al., 2009) with even lower partition coefficients than La and Ce ($D^{cpx/melt}$ (La) ~ 0.05 and $D^{cpx/melt}$ (Ce) ~ 0.086, respectively, Hart and Dunn, 1993). Although Hao et al. (2014) suggested a higher partition coefficient for hydrogen ($D^{peridotite/melt}$ (H_2O) ~ 0.1), this value is still around that of Ce, which suggests that hydrogen reacts rapidly to depletion or enrichment. Furthermore, it is widely accepted that structural hydroxyl content has a great impact on the physical parameters (e.g. lattice-preferred orientation, electrical conductivity) of mantle minerals (e.g. Jung et al., 2006; Selway et al., 2014). Therefore, the relationship between the structural hydroxyl contents and different geochemical and physical variables of NAMs has been widely studied. However, in some cases either no correlation (Falus et al., 2008; Bonadiman et al., 2009; Hao et al., 2016a) or only a weak one has been found (Peslier et al., 2002; Soustelle et al., 2010; Yu et al., 2011; Hao et al., 2012, 2016b; Doucet et al., 2014; Li et al., 2015; Demouchy et al., 2015; Peslier and Bizimis, 2015; Baptiste et al., 2015; Aradi et al., 2017).

The structural hydroxyl contents of clinopyroxenes in NGVF xenoliths, irrespective of their spectral type (1, 2a or 2b) or xenolith group (lherzolitic or wehrlitic series), show no systematic relationship with geochemical and physical parameters (Fig. 5). Similarly, there is no clear link between the structural hydroxyl content of orthopyroxenes and physical variables or equilibration temperatures (Fig. 6a–b). However, a moderate correlation is present between the structural hydroxyl content of orthopyroxenes and certain major elements and heavy rare earth elements (HREE), but only in xenoliths with type 1 orthopyroxene spectra. The trend is positive for Al_2O_3, FeO, CaO, Na_2O, Gd, Tb, Dy, Ho, Er, Tm, Yb, Lu and negative for SiO_2, Cr_2O_3 MgO (Fig. 6c–e). Bulk rock structural hydroxyl contents show no relationship with bulk rock chemistry. However, if we only consider xenoliths where both pyroxenes have type 1 spectra, several correlations with geochemical proxies might be revealed. There are 9 such lherzolite xenoliths among the studied NGVF samples (NMS138, NJS1302, NJS1304, NJS1306, NJS1307, NFK0301, NFL1316, NMC1322, NBN0302A), although these spectrum types are the most prevalent worldwide (Falus et al., 2008; Demouchy et al., 2015; Pintér et al., 2015; Aradi et al., 2017). The most obvious relationships exhibited by these xenoliths are between their bulk structural hydroxyl content and basaltic major elements (Al_2O_3, FeO, CaO, Na_2O), as well as HREE concentrations

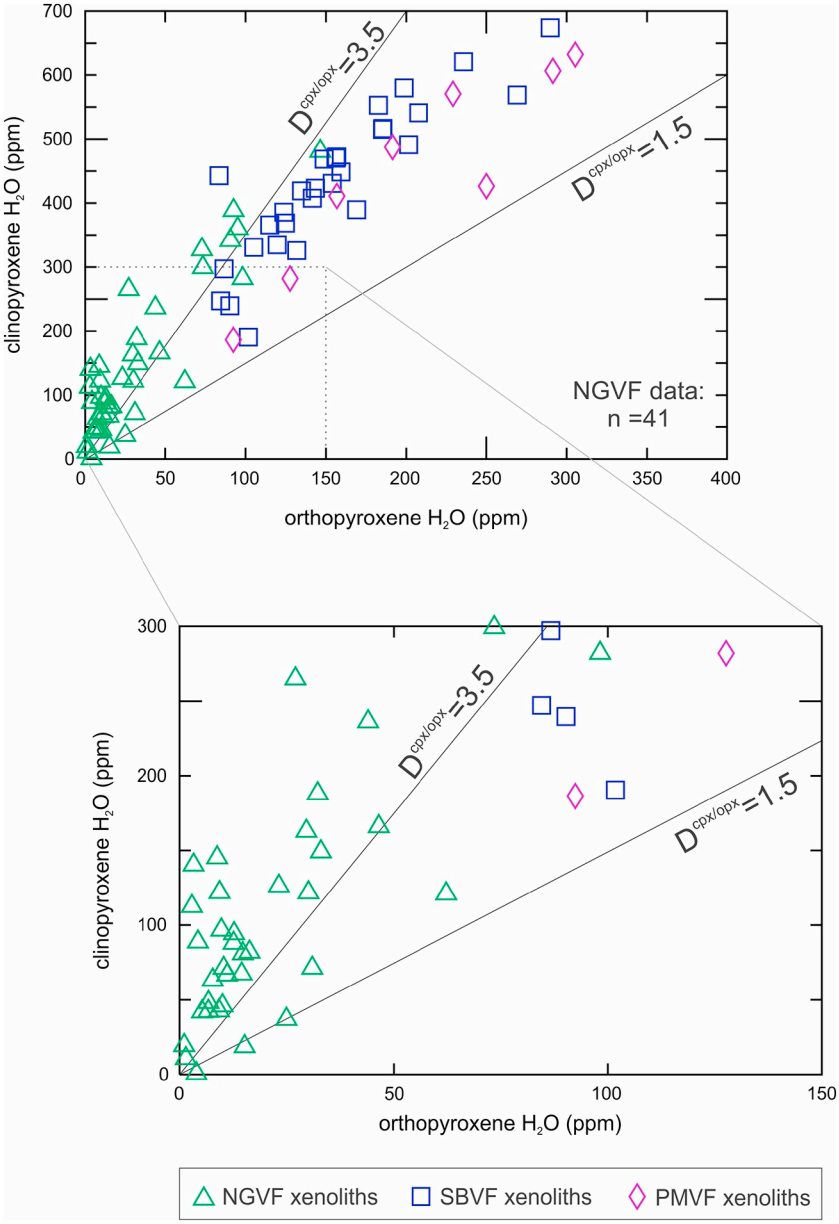

Fig. 4. Partitioning of structural hydroxyl (expressed in H_2O equivalent in ppm wt%) between coexisting clinopyroxene and orthopyroxene ($D^{cpx/opx}$). Trendlines defining 'normal' range are from Xia et al. (2017). Data abbreviations and origin: NGVF - Nógrád-Gömör Volcanic Field (this study), SBVF - Styrian Basin Volcanic Field (Aradi et al., 2017), PMVF - Perşani Mountains Volcanic Field (Falus et al., 2008).

(Fig. 7).

In conclusion, it appears that only pyroxenes with type 1 spectra are likely to represent 'original' or 'equilibrium' conditions after partial melting or metasomatism (presumably under higher water activity). In this case it is anticipated that structural hydroxyl contents must show some correlation with geochemical variables. In contrast, pyroxenes with type 2 spectra may have equilibrated under lower water activity triggered by continental extension, which resulted in the anomalous infrared spectra and also lower structural hydroxyl content. In this latter scenario, only the concentration and the mode of structural hydroxyl incorporation changes, however, other geochemical and petrological features remain more or less the same. It is likely that subsequent metasomatic events could gradually erase these infrared signatures over geological times, resulting in the water content returning to higher concentrations and the infrared spectra to the 'more' common type 1. This may be the reason why these signatures are only preserved in the upper mantle of geologically young extensional basins, which are almost immediately sampled by a subsequent alkaline basaltic volcanic activity. In other areas, perhaps, where the extension is older and more time elapses between the extension and the volcanism bringing up the xenoliths, these signatures may be overwritten and, therefore, will not be preserved. Note that these signatures are not common in upper mantle xenoliths from other alkaline basaltic localities (Styrian Basin and Perşani Mts.) of the Pannonian Basin, where the extension was not significant, and a considerable subduction related flux favored the predominance of type 1 spectra, higher structural hydroxyl contents and more covariance with geochemical proxies (e.g., Falus et al. 2008; Aradi et al., 2017).

7.4. Possible explanations for the low structural hydroxyl contents and anomalous infrared spectra

In the NGVF xenoliths, FTIR results reveal several characteristic spectral features for NAMs:

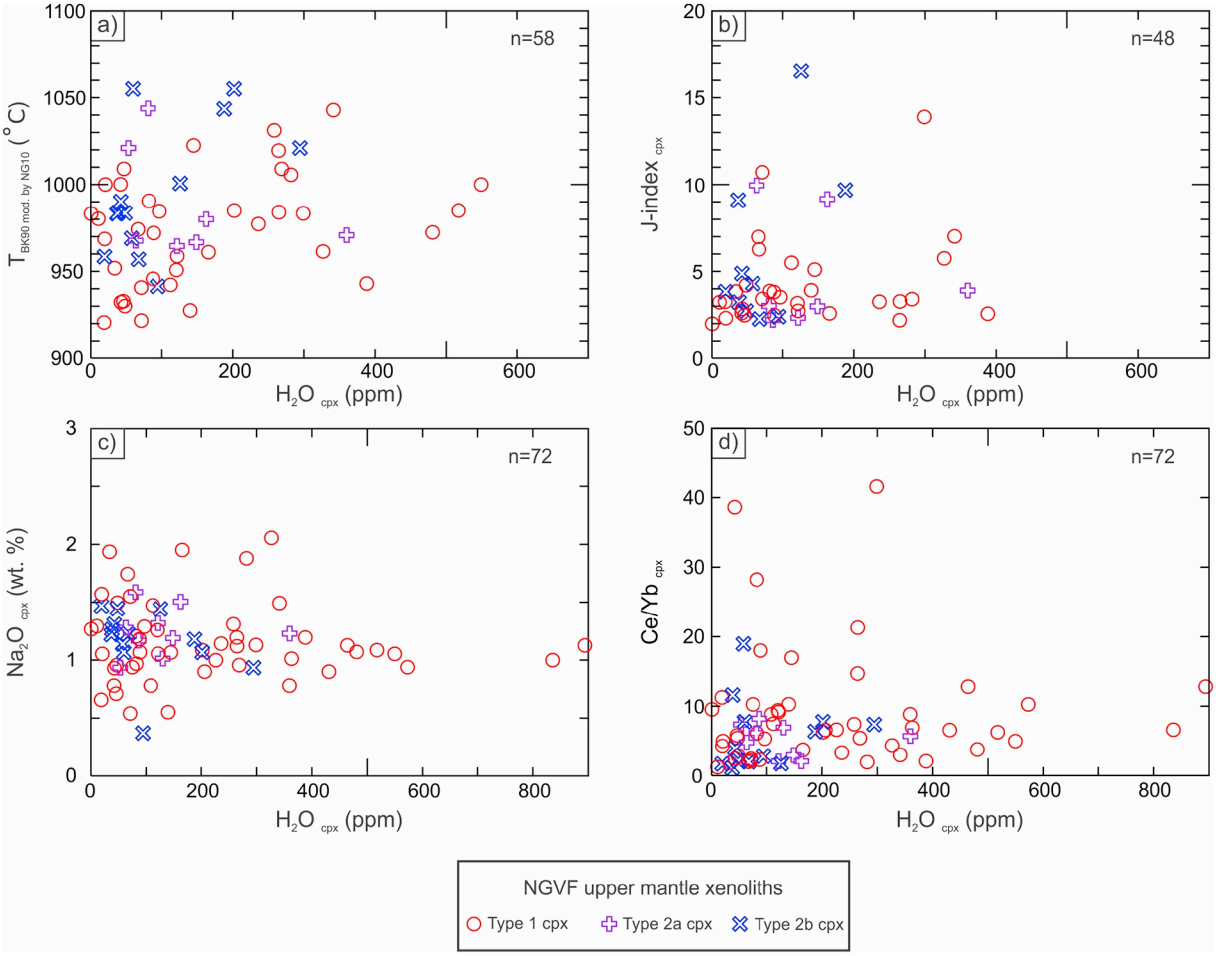

Fig. 5. Structural hydroxyl content (expressed in H_2O equivalent in ppm wt%) compared with different physical and chemical variables of clinopyroxenes. Equilibrium temperature (a), J-index (the volume-averaged integral of the squared orientation densities: for the sake of simplicity its value is 1 for randomly oriented crystal and infinite for single crystals; Bunge, 1982) in clinopyroxenes (b), Na_2O in clinopyroxenes (c) and Ce/Y ratio in clinopyroxenes (d) versus structural hydroxyl content of clinopyroxenes. The equilibrium temperature and the geochemical data of the clinopyroxenes (Supplementary Table 2) are from Liptai et al. (2017). Note that the quality of the J-index results (Supplementary Table 2) is not always excellent because of the restricted number of clinopyroxene grains within a xenolith. Equilibrium temperature calculations are based on the method of Brey and Köhler (1990) modified by Nimis and Grütter (2010). Different spectrum types are depicted with distinct symbols.

a) Although most of the stretching bands of structural hydroxyl on FTIR spectra appear at well-known wavenumbers (Table 1), their relative intensities are often anomalous. The most intense bands appear only at lower wavenumbers (Fig. 2), whereas usually, the bands at the highest wavenumber commonly are the most intense ones (e.g. Pintér et al., 2015; Denis et al., 2015; Demouchy et al., 2015; Aradi et al., 2017).
b) The structural hydroxyl content of all NAMs is extremely low compared to those in other spinel facies upper mantle xenoliths from elsewhere in the Pannonian Basin (Falus et al., 2008, Aradi et al., 2017) or other off-craton occurrences (Peslier, 2010) (Fig. 3). Histograms of structural hydroxyl contents with respect to spectrum types for orthopyroxenes (Fig. 2b) reveal that xenoliths with type 1 orthopyroxene spectra show a wider and more uniform distribution of structural hydroxyl concentration, resulting in higher average contents. In contrast, xenoliths with type 2a and 2b orthopyroxenes have dominantly lower contents of structural hydroxyl (62 and 71% of type 2a and 2b orthopyroxenes < 20 ppm, respectively). This implies an apparent link between spectral features and structural hydroxyl concentrations. This link is even more obvious for clinopyroxenes (Fig. 2c). Type 1 clinopyroxenes have a much wider distribution of concentrations and the highest proportion of samples with > 200 ppm structural hydroxyl (46%). In contrast, both type 2 clinopyroxenes have structural hydroxyl contents dominantly below 200 ppm (89 and 84%, respectively). Interestingly, for type 2a clinopyroxenes, there are no xenoliths with structural hydroxyl content below 50 ppm, whereas type 2b clinopyroxenes show mainly these low values (38%) (Fig. 2c). In other words, the weaker the band at ~3630 cm^{-1}, the lower the structural hydroxyl concentration in clinopyroxene just like in case of type 1 clinopyroxenes. The same applies for orthopyroxenes with the band at 3600 cm^{-1}.
c) The partition coefficient for structural hydroxyl between pyroxenes is dominantly higher than the range defined as 'normal' by Xia et al. (2017) (Fig. 4), which means that clinopyroxene contains significantly more structural hydroxyl than the coexisting orthopyroxene (D > 3.5).
d) The structural hydroxyl content and different physico-chemical variables show limited or no correlation (Fig. 5; 6).

Below it will be discussed what mechanism(s) might lead to the spectral characteristics of structural hydroxyl in upper mantle xenoliths from the NGVF.

7.4.1. The role of lower water activity

7.4.1.1. Extension. The major difference between the NGVF and other

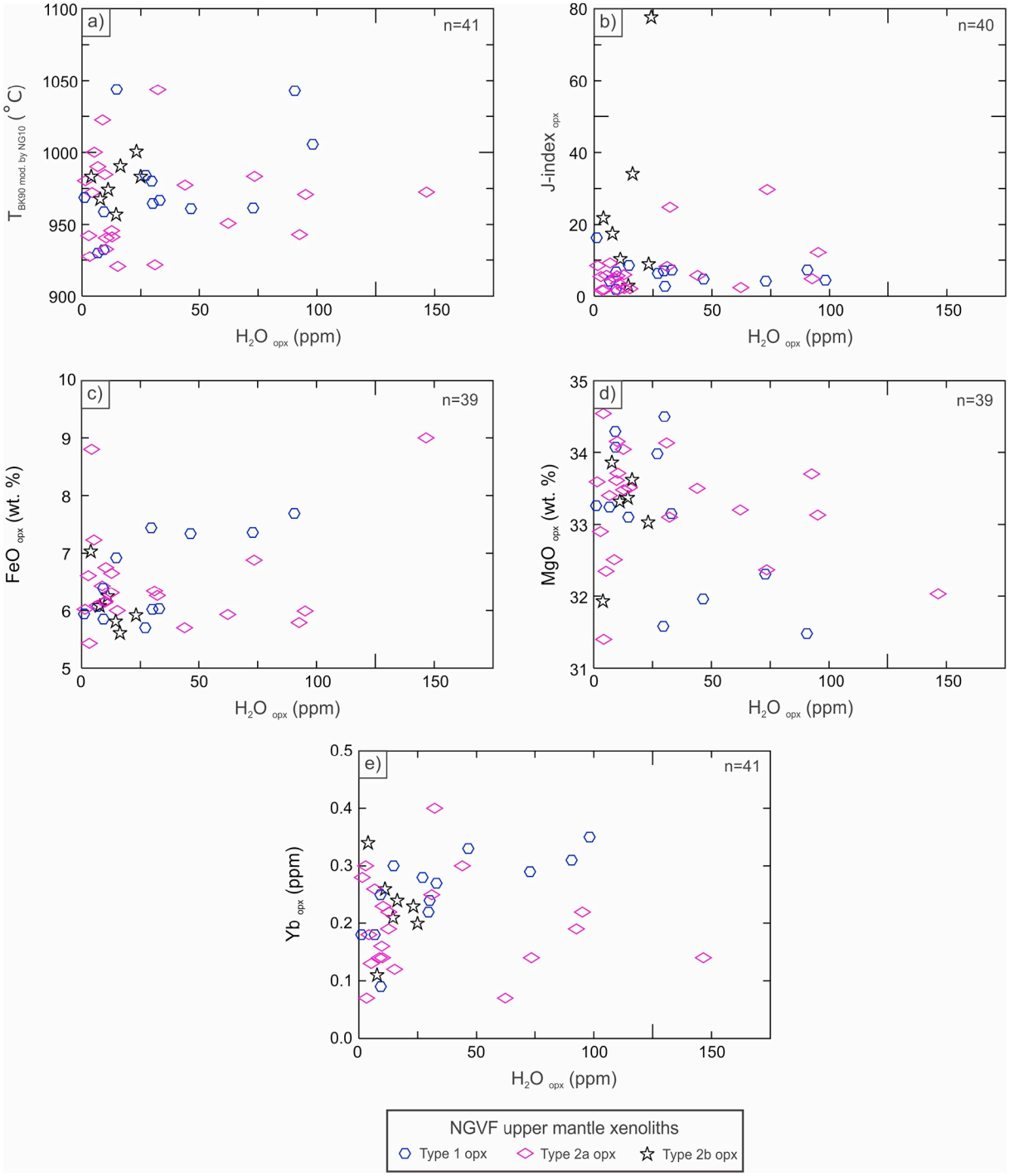

Fig. 6. Different physical-chemical variables versus the structural hydroxyl content (expressed in H_2O equivalent in ppm wt%) of orthopyroxenes. Equilibrium temperature (a), J-index in orthopyroxenes (b), FeO in orthopyroxenes (c), MgO in orthopyroxenes (d) and Yb in orthopyroxenes (e) versus structural hydroxyl content of orthopyroxenes. The equilibrium temperature and the geochemical data of the orthopyroxenes (Supplementary Table 2) are from Liptai et al. (2017). Note that the quality of the J-index results (Supplementary Table 2) are not always excellent because of the restricted number of orthopyroxene grains within a xenolith. The equilibrium temperature calculations are based on the method of Brey and Köhler (1990) modified by Nimis and Grütter (2010). The different spectrum types depicted with distinct symbols.

marginal localities from where information on structural hydroxyl contents of NAMs in upper mantle peridotites is available (i.e. Perşani Mts. and Styrian Basin localities) is that these localities were affected by subduction-related processes (e.g. Falus et al., 2008; Aradi et al., 2017) and the extent of Miocene extension is only moderate (Horváth, 1993). In the NGVF, however, the role of subduction is disputed (Szafián et al., 1997) and the impact of Miocene extension is more significant (Horváth, 1993). It is logical to assume that the more significant extension (i.e. higher thinning factor and shallower lithosphere-asthenosphere boundary depth) may be a factor in the formation of these characteristic infrared features. During extension, a significant portion of the upper mantle is placed under significantly lower pressure, which affects both the asthenosphere and the lithospheric mantle. The structural hydroxyl groups in NAMS presumably may reach

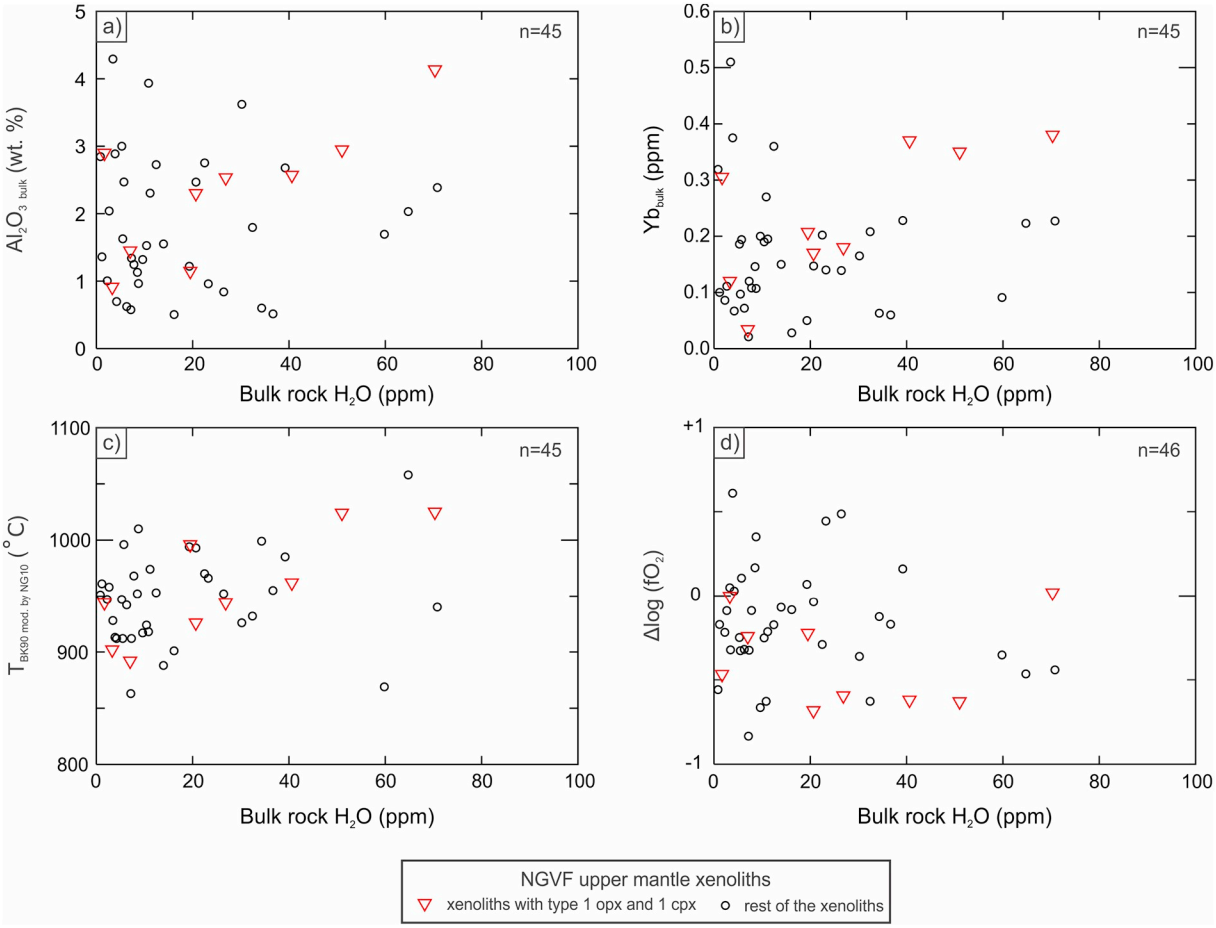

Fig. 7. Different physical-chemical variables versus the hydroxyl content (expressed in H_2O equivalent in ppm wt%) of the bulk rock. Al_2O_3 in bulk rocks (a), Yb in bulk rocks (b), equilibrium temperature (c) and FMQ (fayalite-magnetite-quartz) buffered oxygen fugacity (fO_2) values (d) versus structural hydroxyl content of bulk rocks. The equilibrium temperature and the geochemical data (Supplementary Table 2) are from Liptai et al. (2017). The equilibrium temperature calculations are based on the method of Brey and Köhler (1990) modified by Nimis and Grütter (2010). The oxygen fugacity was calculated using the oxygen barometer of Ballhaus et al. (1991) (Supplementary Table 2). Xenoliths with both type 1 clinopyroxenes and orthopyroxenes were highlighted using red triangles. Three xenoliths (NMS1304, NFL1324, NFL1326) are not shown here due to their high bulk rock structural hydroxyl content. (For interpretation of the references to color in this figure legend, the reader is referred to the web version of this article.)

new equilibrium under these changed physico-chemical conditions, which results in lower structural hydroxyl contents and anomalous infrared spectra (Fig. 8).

One potential factor could be the lowered activity of water at lower pressures. The changing water activity (in the absence of percolating fluids) changes the structural hydroxyl content of NAMs as the solubility of 'water' in NAMs is proportional to the activity of water (e.g. Bali et al., 2008). This means that the lower activity of water lowers the structural hydroxyl concentrations in NAMs if other physico-chemical properties are unchanged. It has been recently shown for olivine that different substitution mechanisms of structural hydroxyl may have different dependency on water activity (e.g. Tollan et al., 2017). It follows that changing the activity of water may not only increase or lower the structural hydroxyl content but can also alter the relative proportions of absorption bands (i.e. the infrared spectra will be changed). The new equilibrium under lower activity (due to extension), therefore may account for the lower structural hydroxyl contents and the different contribution of various substitution mechanisms (Fig. 8). Consequently, the observed signatures in the concentration and incorporation mechanism of structural hydroxyl groups may be characteristic for young extensional areas, where the upper mantle experienced significant uplift and thinning. The fact that the upper mantle xenoliths from NGVF usually show these signatures, unlike those from marginal areas of CPR (Falus et al., 2008; Aradi et al., 2017), implies that the process(es) responsible affected the entire NGVF: extension could clearly be such a process.

7.4.1.2. Possible role of 'dry' metasomatic agents. The Neogene evolution of the CPR was accompanied by compositionally variable (silicic, calc-alkaline and alkali mafic) volcanism all over the region (e.g. Szabó et al., 1992). Among these magmatic events, the products of calc-alkaline and alkali mafic activity appear in the NGVF (Fig. 1b) and probably affected the characteristics of the local upper mantle. The migration of melts can either modify or leave unchanged the structural hydroxyl content of the upper mantle, depending on the water activity in the melt agent. The low structural hydroxyl contents of the studied xenoliths (Table 1) potentially calls for a migrating melt with low water activity. However, based on the presence of almandine garnets in andesite, Harangi et al. (2001) implied a water-rich melt, which requires a hydrous mantle source for the calc-alkaline volcanism. Furthermore, the evolution of such a melt, which would lower the water activity, presumably happened only at crustal levels due to high-pressure fractionation and contamination (Harangi et al., 2001). In contrast, for the alkali basaltic volcanic activity, Zajacz et al. (2007) proposed that the evolution of the assumed parental melt took place well below the Moho. Dissolved volatiles, especially CO_2, can also significantly influence the water activity in melts. According to experiments, the higher the CO_2 content of a melt, the lower its

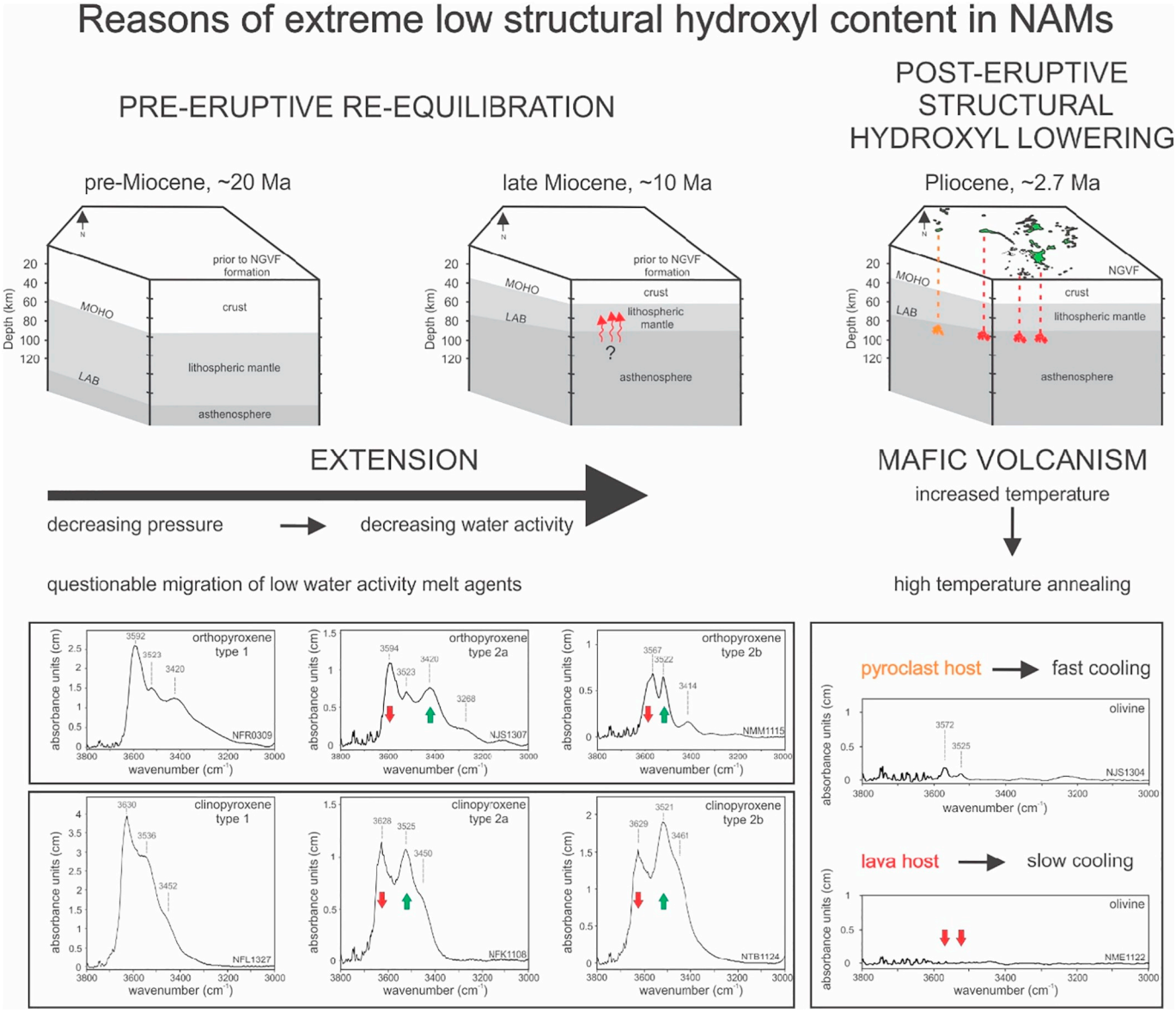

Fig. 8. Simplified cartoon on the possible pre-, syn- or post-eruptive processes, which modified the FTIR spectra characteristics and lowered the structural hydroxyl contents in NAMs of Nógrád-Gömör upper mantle xenoliths. The depth of the local Moho and the lithosphere-asthenosphere boundary (LAB) are based on the results of Klébesz et al. (2015). The distribution of the basalts is based on Jugovics (1971).

water activity (e.g. Sokol et al., 2013). The presence of abundant primary CO_2 fluid inclusions in metasomatized Nógrád-Gömör xenoliths (Szabó and Bodnar, 1996, 1998) suggests that great amounts of CO_2 were previously dissolved in the melt, and therefore its water activity was probably low. Indeed, the calculated CO_2 contents (1.27–1.94 wt%) are significantly higher than the measured H_2O concentrations (0.14–0.67 wt%) in silicate melt inclusions that probably represent the metasomatic agent (Szabó et al., 1996).

The young alkali basaltic volcanic activity, which took place in the last 7 million years (Hurai et al., 2013) lead to the formation of maars, diatremes, tuff cones, cinder/spatter cones and lava flows on the surface (e.g., Konečný et al., 1995) and extensive mantle metasomatism (Szabó and Taylor, 1994; Patkó et al., 2013; Liptai et al., 2017), and significant underplating (Kovács et al., 2004; Zajacz et al., 2007) at great depths is the best candidate for a 'dry' metasomatism. Since this is the last magmatic event before the entrainment of the xenoliths it may have overprinted the signatures of older episodes such as the calc-alkaline volcanism. The observed heterogeneities of structural hydroxyl contents (Table 1) and variabilities in spectral features may also be explained by the different stages of complete re-equilibration caused by 'dry' metasomatism (Fig. 8). However, note that the dimension of such a 'dry' metasomatic event is restricted to the melt migration paths and their close environment, and a regional effect is unlikely as it is suggested by the distribution of wehrlite xenoliths (Patkó et al., 2013) or long period magnetotellurics (Novák et al., 2014).

7.4.2. *Temperature-driven annealing*

Another possible mechanism for lowering the structural hydroxyl content is temperature-driven annealing. At high pressures typical for the upper mantle, significant structural hydroxyl loss from NAMs is possible through high degrees of partial melting, which is triggered by significantly elevated temperatures. There is, however, no evidence for anomalously high degree of partial melting beneath the studied volcanic area (Liptai et al., 2017). Consequently, we exclude that the relatively low structural hydroxyl contents in pyroxenes are due to temperature driven structural hydroxyl loss at upper mantle depth. The fact that the activity of water increases with temperature at such pressures (e.g. Bali et al., 2008) also makes this scenario rather unlikely. In

addition, the effect of extension was probably more significant and straightforward on the pressure, whereas temperature may have been less capable to achieve the new equilibrium conditions (i.e. convective heat transfer) relative to the almost 'instant' drop in pressure.

Lowering of the structural hydroxyl content related to elevated temperatures could also occur in xenoliths while being carried by the host magma during ascent. Peslier and Luhr (2006) pointed out that xenoliths may lose significant proportions of their structural hydroxyl content this way, especially in case of an alkali basalt host, which moves more slowly than lamprophyre or kimberlite magmas (Kelley and Wartho, 2000) (i.e. xenoliths spend more time at elevated temperatures). The calculated ascent rate for the alkali basalt magma in the NGVF is only 0.1 ms^{-1} beneath the Moho, and 5 ms^{-1} in the crust (Szabó and Bodnar, 1996). For the reasons outlined above, the diffusional loss of structural hydroxyl – especially in olivine, in which the speed of diffusion is fastest – is suggested to happen at very shallow depths or on the surface only, where the activity of water is sufficiently low (Ferriss et al., 2016; Tian et al., 2017). The upper mantle xenoliths entrained in other alkali basalts with probably similar ascent rates in the CPR (i.e. Perşani Mts. and Styrian Basin) contain appreciable amounts of structural hydroxyl. This fact makes it rather unlikely that decrease in structural hydroxyl content during ascent could be the only explanation for the dry olivines in the NGVF NAMs. Consequently, another explanation should also be considered. In the NGVF, the alkali basalt volcanism produced several volcanic edifices including maars, diatremes, tuff cones, cinder/spatter cones and lava flows (Konečný et al., 1995). The numerous slowly cooling lava flows built several 'massive' basalt plateaus (e.g. Medves Plateau; Fig. 1b), except at the Jelšovec locality, where the host rock is pyroclastic, forming a maar. Xenoliths from Jelšovec are the only samples in the NGVF that contain detectable amounts of structural hydroxyl in olivines and higher concentration in other NAMs, and their structural hydroxyl contents are the highest (Table 1). Accordingly, we suggest that the type of the host rock (i.e. pyroclast vs. 'massive' lava flow) plays a significant role in modifying the structural hydroxyl content. This assumption is supported by the fact that olivines carrying structural hydroxyl in upper mantle xenoliths from other volcanic fields of the CPR (i.e., Stryian Basin and Perşani Mts.) are also hosted predominantly in pyroclastic successions (Falus et al., 2008; Aradi et al., 2017). In conclusion, xenoliths in pyroclastic rocks appear to preserve their 'original' structural hydroxyl content better than those in lavas. This is due to the faster cooling rate of pyroclastics compared to 'massive' lava flows where the temperature could remain high enough for a longer period of time. Similar conclusions also have been drawn by Lloyd et al. (2016) and Biró et al. (2016). They found that clinopyroxene and quartz phenocrysts in different volcanic formations show higher structural hydroxyl contents and are closer to equilibrium with their host rocks in volcanic successions, which went through rapid cooling after deposition (i.e. volcanic ash, pyroclastic deposits and basal layers of ignimbrites). The time-span for post-deposition cooling (weeks, maybe months) in most cases is only enough to change the structural hydroxyl content in olivines, in which the diffusion is fast (10^{-11}–10^{-9} m^2/s at 1100 °C; Tian et al., 2017), but not enough to trigger significant modification in the pyroxenes, in which diffusion is slower (10^{-14}–10^{-11} m^2/s at 1100 °C; Tian et al., 2017). Hence, the low structural hydroxyl content in pyroxenes is unlikely to have been reset during syn- and post-eruption periods, but more likely is related to the extension in the NGVF as outlined above. In our interpretation, the olivines are highly sensitive indicators of syn- and post-eruptive loss of structural hydroxyl (Fig. 8). Consequently, the presence of 'dry' olivines in the investigated upper mantle xenoliths may indicate that considerable loss of hydrogen may have taken place during the post-depositional slow cooling of lava flows in the NGVF. To our knowledge, our study is among the first ones to report that post-eruptive thermal history of xenoliths in their host rocks could influence the structural hydroxyl contents of NAMs, especially that of olivine. Note that similar conclusions were drawn in case of the fast-diffusing Li based on upper mantle xenolith constituent separates (Ionov and Seitz, 2008). This suggests that before collecting suitable upper mantle xenoliths for estimating the fast-diffusing element contents including hydrogen, it is important to consider the physical volcanological features and select parts of volcanic formations/successions, which are characterized by fast cooling rates (fall deposits, basal layers of pyroclasts etc.).

7.4.3. Oxidation

Theoretically, oxidation caused by the host magma can also lead to low structural hydroxyl contents in xenoliths (Peslier et al., 2002). The oxygen fugacity (fO_2) values of the NGVF xenoliths compared to the FMQ (fayalite-magnetite-quartz) buffer, calculated using the oxygen barometer of Ballhaus et al. (1991), are between -0.8 ± 0.7 log units (with an average of ~ -0.2) (Supplementary Table 2), which is within the range of -1.5 to $+1.5$ log units defined as typical for peridotite xenoliths (Wood et al., 1990). The Fe^{2+} and Fe^{3+} distribution for spinel was calculated based on the spinel stoichiometry. The fO_2 values show no relationship with the structural hydroxyl contents (Fig. 7d). This implies that oxidation-related modification of structural hydroxyl contents probably did not occur in the upper mantle nor during entrainment in the host magma.

Degassing can increase the fO_2 of the magma if H_2O and CO_2 are the dominant volatile elements of it (Brounce et al., 2017), hence pyroclasts usually represent more oxidizing environments compared to lava rocks in basaltic systems. Furthermore, the generation of the Jelšovec maar is a result of phreatic/phreatomagmatic activity (Konečný et al., 1995), which also suggests oxidative circumstances in its formation. Consequently, if oxidation had a significant effect on the structural hydroxyl concentration, then the Jelšovec xenoliths, the only ones hosted in pyroclastics in the study area, should be the driest. In contrast, the Jelšovec xenoliths have the highest structural hydroxyl contents (Table 1). These observations suggest that the late oxidation of the host rock may have no significant effect on the structural hydroxyl content of the NGVF xenoliths.

8. Summary

We carried out a detailed FTIR study on the NAMs of 63 upper mantle xenoliths from the NGVF with well-defined petrography, geochemistry and physical characteristics. The FTIR results reveal several unusual features including anomalous spectra of upper mantle silicates, extremely low contents of structural hydroxyl and widely variable partition coefficients between pyroxenes. Moreover, the structural hydroxyl contents show limited or no correlation with different geochemical (e.g. major and trace elements) and physical (e.g. fabric strength) variables. All these observations can be interpreted as results of lowered water activity due to young extension (reflected especially in pyroxenes). In addition, interaction of a metasomatic agent having low water activity cannot be ruled out. In our interpretation, the extremely 'dry' nature of olivines, relative to other marginal localities in the Carpathian-Pannonian region, may be attributed to the slow cooling of 'massive' basaltic lava flows enclosing the xenoliths. The very slow post-depositional cooling could in these cases have led to significant loss of structural hydroxyl from olivine, in which the diffusion of structural hydroxyl is rapid compared to pyroxenes.

The novel applications of our study include the introduction of the diagnostic features (low structural hydroxyl content, anomalous partitioning between pyroxenes and anomalous relative absorbances of characteristic bands in pyroxenes), which can be used to detect re-equilibration under lower water activity in young extensional tectonic settings. Dry olivines could be used as an indicator that significant post-depositional loss of structural hydroxyl occurred in slowly cooling massive lava flows. This experience could help in selecting more suitable volcanic formations (pyroclasts) for obtaining representative structural hydroxyl content of NAMs for the upper mantle.

Supplementary data to this article can be found online at https://doi.org/10.1016/j.chemgeo.2018.12.017.

Acknowledgements

The authors are grateful to Csaba Németh for his help with FTIR measurements in the Research Centre for Natural Sciences of the Hungarian Academy of Sciences in Budapest. The authors also owe thanks to Norman J. Pearson and David Adams for their assistance in FTIR analyses at Macquarie University. The analytical data were obtained using instrumentation funded by DEST Systemic Infrastructure Grants, ARC LIEF, NCRIS/AuScope, industry partners and Macquarie University. The authors are grateful to the Lithosphere Fluid Research Lab (LRG) of the Eötvös Loránd University to provide appropriate circumstances for doing research. Sonja Aulbach is thanked for her constructive comments and thorough structural shaping of the paper. This project has been implemented with the support provided to I. J. K. from the National Research, Development and Innovation Fund of Hungary, financed under the K128122 funding scheme and the Bolyai Postodoctoral Fellowship program of the Hungarian Academy of Sciences. The study was also supported by a Lendület Research Grant to the MTA CSFK Lendület Pannon LitH_2Oscope Research group. The work was further supported by the Marie Curie International Reintegration Grant (NAMS-230937) of I.J.K. The FTIR spectra are available on the PULI (Pannonian Uniform Lithospheric Infrared spectral database) website (http://puli.mfgi.hu/). This is the 88th publication of the Lithosphere Fluid Research Lab (LRG). This is contribution 1239 from the ARC Centre of Excellence for Core to Crust Fluid Systems (http://www.ccfs.mq.edu.au) and 1278 in the GEMOC Key Centre (http://www.gemoc.mq.edu.au).

References

Aizawa, Y., Barnhoorn, A., Faul, U.H., Fitz Gerald, J.D., Jackson, I., Kovács, I., 2008. Seismic properties of Anita Bay dunite: an exploratory study of the influence of water. J. Petrol. 49 (4), 841–855.
Aradi, L.E., Hidas, K., Kovács, I.J., Tommasi, A., Klébesz, R., Garrido, C.J., Szabó, C., 2017. Fluid-enhanced annealing in the subcontinental lithospheric mantle beneath the westernmost margin of the Carpathian-Pannonian extensional basin system. Tectonics 36, 2987–3011.
Aubaud, C., Hauri, E.H., Hirschmann, M.M., 2004. Hydrogen partition coefficients between nominally anhydrous minerals and basaltic melts. Geophys. Res. Lett. 31 (20).
Bada, G., Horváth, F., 2001. On the structure and tectonic evolution of the Pannonian basin and surrounding orogens. Acta Geol. Hung. 44 (2), 301–327.
Bali, E., Bolfan-Casanova, N., Koga, K.T., 2008. Pressure and temperature dependence of H solubility in forsterite: an implication to water activity in the Earth interior. Earth Planet. Sci. Lett. 268 (3–4), 354–363.
Balla, Z., 1984. The Carpathian loop and the Pannonian basin: a kinematic analysis. Geophys. Trans. 30, 313–353.
Ballhaus, C., Berry, R.F., Green, D.H., 1991. High pressure experimental calibration of the olivine-orthopyroxene-spinel oxygen geobarometer: implications for the oxidation state of the upper mantle. Contrib. Mineral. Petrol. 107 (1), 27–40.
Baptiste, V., Tommasi, A., Vauchez, A., Demouchy, S., Rudnick, R.L., 2015. Deformation, hydration, and anisotropy of the lithospheric mantle in an active rift: constraints from mantle xenoliths from the North Tanzanian Divergence of the East African Rift. Tectonophysics 639, 34–55.
Bell, D.R., Rossman, G.R., 1992. Water in Earth's mantle: the role of nominally anhydrous minerals. Science 255 (5050), 1391–1397.
Bell, D.R., Ihinger, P.D., Rossman, G.R., 1995. Quantitative analysis of trace OH in garnet and pyroxenes. Am. Mineral. 80 (5–6), 465–474.
Bell, D.R., Rossman, G.R., Maldener, J., Endisch, D., Rauch, F., 2003. Hydroxide in olivine: A quantitative determination of the absolute amount and calibration of the IR spectrum. J. Geophys. Res. Solid Earth 108 (B2).
Beran, A., Putnis, A., 1983. A model of the OH positions in olivine, derived from infrared-spectroscopic investigations. Phys. Chem. Miner. 9 (2), 57–60.
Berkesi, M., Hidas, K., Guzmics, T., Dubessy, J., Bodnar, R.J., Szabo, C., Vajna, B., Tsunogae, T., 2009. Detection of small amounts of H_2O in CO_2-rich fluid inclusions using Raman spectroscopy. J. Raman Spectrosc. 40 (11), 1461–1463.
Berry, A.J., Hermann, J., O'Neill, H.S., Foran, G.J., 2005. Fingerprinting the water site in mantle olivine. Geology 33 (11), 869–872.
Biró, T., Kovács, I.J., Király, E., Falus, G., Karátson, D., Bendő, Z., Fancsik, T., Sándorné, J.K., 2016. Concentration of hydroxyl defects in quartz from various rhyolitic ignimbrite horizons: results from unpolarized micro-FTIR analyses on unoriented phenocryst fragments. Eur. J. Mineral. 28 (2), 313–327.
Bollinger, C., Raterron, P., Cordier, P., Merkel, S., 2014. Polycrystalline olivine rheology in dislocation creep: revisiting experimental data to 8.1 GPa. Phys. Earth Planet. Inter. 228, 211–219.
Bonadiman, C., Hao, Y., Coltorti, M., Dallai, L., Faccini, B., Huang, Y., Xia, Q., 2009. Water contents of pyroxenes in intraplate lithospheric mantle. Eur. J. Mineral. 21 (3), 637–647.
Brey, G.P., Köhler, T., 1990. Geothermobarometry in four-phase lherzolites II. New thermobarometers, and practical assessment of existing thermobarometers. J. Petrol. 31 (6), 1353–1378.
Brounce, M., Stolper, E., Eiler, J., 2017. Redox variations in Mauna Kea lavas, the oxygen fugacity of the Hawaiian plume, and the role of volcanic gases in Earth's oxygenation. Proc. Natl. Acad. Sci. 114 (34), 8997–9002.
Bunge, H.J., 1982. Texture Analysis in Materials Sciences. Buttleworth, London.
Csontos, L., Nagymarosy, A., 1998. The Mid-Hungarian line: a zone of repeated tectonic inversions. Tectonophysics 297 (1), 51–71.
Csontos, L., Vörös, A., 2004. Mesozoic plate tectonic reconstruction of the Carpathian region. Palaeogeogr. Palaeoclimatol. Palaeoecol. 210 (1), 1–56.
Csontos, L., Nagymarosy, A., Horváth, F., Kovac, M., 1992. Tertiary evolution of the Intra-Carpathian area: a model. Tectonophysics 208 (1–3), 221–241.
Della Ventura, G., Oberti, R., Hawthorne, F.C., Bellatreccia, F., 2007. FTIR spectroscopy of Ti-rich pargasites from Lherz and the detection of O_2-at the anionic O_3 site in amphiboles. Am. Mineral. 92 (10), 1645–1651.
Demouchy, S., Bolfan-Casanova, N., 2016. Distribution and transport of hydrogen in the lithospheric mantle: a review. Lithos 240, 402–425.
Demouchy, S., Tommasi, A., Barou, F., Mainprice, D., Cordier, P., 2012. Deformation of olivine in torsion under hydrous conditions. Phys. Earth Planet. Inter. 202, 56–70.
Demouchy, S., Ishikawa, A., Tommasi, A., Alard, O., Keshav, S., 2015. Characterization of hydration in the mantle lithosphere: peridotite xenoliths from the Ontong Java Plateau as an example. Lithos 212, 189–201.
Demouchy, S., Shcheka, S., Denis, C.M., Thoraval, C., 2017. Subsolidus hydrogen partitioning between nominally anhydrous minerals in garnet-bearing peridotite. Am. Mineral. 102 (9), 1822–1831.
Denis, C.M., Demouchy, S., Shaw, C.S., 2013. Evidence of dehydration in peridotites from Eifel Volcanic Field and estimates of the rate of magma ascent. J. Volcanol. Geotherm. Res. 258, 85–99.
Denis, C.M., Alard, O., Demouchy, S., 2015. Water content and hydrogen behaviour during metasomatism in the uppermost mantle beneath Ray Pic volcano (Massif Central, France). Lithos 236, 256–274.
Denis, C.M., Demouchy, S., Alard, O., 2018. Heterogeneous hydrogen distribution in orthopyroxene from veined mantle peridotite (San Carlos, Arizona): Impact of melt-rock interactions. Lithos 302–303, 298–311.
Doucet, L.S., Peslier, A.H., Ionov, D.A., Brandon, A.D., Golovin, A.V., Goncharov, A.G., Ashchepkov, I.V., 2014. High water contents in the Siberian cratonic mantle linked to metasomatism: an FTIR study of Udachnaya peridotite xenoliths. Geochim. Cosmochim. Acta 137, 159–187.
Embey-Isztin, A., Downes, H., James, D.E., Upton, B.G.J., Dobosi, G., Ingram, G.A., Harmon, R.S., Scharbert, H.G., 1993. The petrogenesis of Pliocene alkaline volcanic rocks from the Pannonian Basin, Eastern Central Europe. J. Petrol. 34 (2), 317–343.
Falus, G., Tommasi, A., Ingrin, J., Szabó, C., 2008. Deformation and seismic anisotropy of the lithospheric mantle in the southeastern Carpathians inferred from the study of mantle xenoliths. Earth Planet. Sci. Lett. 272 (1), 50–64.
Ferriss, E., Plank, T., Walker, D., 2016. Site-specific hydrogen diffusion rates during clinopyroxene dehydration. Contrib. Mineral. Petrol. 171 (6), 55.
Girard, J., Chen, J., Raterron, P., Holyoke, C.W., 2013. Hydrolytic weakening of olivine at mantle pressure: evidence of [100](010) slip system softening from single-crystal deformation experiments. Phys. Earth Planet. Inter. 216, 12–20.
Green, D.H., Hibberson, W.O., Kovács, I., Rosenthal, A., 2010. Water and its influence on the lithosphere-asthenosphere boundary. Nature 467 (7314), 448–451.
Gu, X., Ingrin, J., Deloule, E., France, L., Xia, Q., 2018. Metasomatism in the sub-continental lithospheric mantle beneath the south French Massif Central: Constraints from trace elements, Li and H in peridotite minerals. Chem. Geol. 478, 2–17.
Hao, Y., Xia, Q., Liu, S., Feng, M., Zhang, Y., 2012. Recognizing juvenile and relict lithospheric mantle beneath the North China Craton: Combined analysis of H_2O, major and trace elements and Sr–Nd isotope compositions of clinopyroxenes. Lithos 149, 136–145.
Hao, Y., Xia, Q., Li, Q., Chen, H., Feng, M., 2014. Partial melting control of water contents in the Cenozoic lithospheric mantle of the Cathaysia block of South China. Chem. Geol. 380, 7–19.
Hao, Y.T., Xia, Q.K., Jia, Z.B., Zhao, Q.C., Li, P., Feng, M., Liu, S.C., 2016a. Regional heterogeneity in the water content of the Cenozoic lithospheric mantle of Eastern China. J. Geophys. Res. Solid Earth 121 (2), 517–537.
Hao, Y.T., Xia, Q.K., Tian, Z.Z., Liu, J., 2016b. Mantle metasomatism did not modify the initial H_2O content in peridotite xenoliths from the Tianchang basalts of eastern China. Lithos 260, 315–327.
Harangi, S., 2001. Neogene to Quaternary volcanism of the Carpathian–Pannonian Region—a review. Acta Geol. Hung. 44 (2), 223–258.
Harangi, S.Z., Downes, H., Kósa, L., Szabó, C.S., Thirlwall, M.F., Mason, P.R.D., Mattey, D., 2001. Almandine garnet in calc-alkaline volcanic rocks of the Northern Pannonian Basin (Eastern–Central Europe): Geochemistry, petrogenesis and geodynamic implications. J. Petrol. 42 (10), 1813–1843.
Harangi, S., Jankovics, M.É., Sági, T., Kiss, B., Lukács, R., Soós, I., 2015. Origin and geodynamic relationships of the Late Miocene to Quaternary alkaline basalt volcanism in the Pannonian basin, eastern–Central Europe. Int. J. Earth Sci. 104 (8), 2007–2032.
Hart, S.R., Dunn, T., 1993. Experimental cpx/melt partitioning of 24 trace elements. Contrib. Mineral. Petrol. 113 (1), 1–8.
Hauri, E.H., Gaetani, G.A., Green, T.H., 2006. Partitioning of water during melting of the

Earth's upper mantle at H 2 O-undersaturated conditions. Earth Planet. Sci. Lett. 248 (3), 715–734.
Hidas, K., Guzmics, T., Szabó, Cs, Kovács, I., Bodnar, R.J., Zajacz, Z., Nédli, Zs, Vaccari, L., Perucchi, A., 2010. Coexisting silicate melt inclusions and H_2O-bearing, CO_2-rich fluid inclusions in mantle peridotite xenoliths from the Carpathian–Pannonian region (central Hungary). Chem. Geol. 274 (1), 1–18.
Hirschmann, M.M., Tenner, T., Aubaud, C., Withers, A.C., 2009. Dehydration melting of nominally anhydrous mantle: the primacy of partitioning. Phys. Earth Planet. Inter. 176 (1–2), 54–68.
Horváth, F., 1993. Towards a mechanical model for the formation of the Pannonian basin. Tectonophysics 226 (1–4), 333–357.
Houseman, G.A., Gemmer, L., 2007. Intra-orogenic extension driven by gravitational instability: Carpathian-Pannonian orogeny. Geology 35 (12), 1135–1138.
Huismans, R.S., Podladchikov, Y.Y., Cloetingh, S., 2001. Dynamic modeling of the transition from passive to active rifting, application to the Pannonian basin. Tectonics 20 (6), 1021–1039.
Hurai, V., Danišík, M., Huraiová, M., Paquette, J.L., Ádám, A., 2013. Combined U/Pb and (U–Th)/He geochronometry of basalt maars in Western Carpathians: implications for age of intraplate volcanism and origin of zircon metasomatism. Contrib. Mineral. Petrol. 166 (4), 1235–1251.
Ingrin, J., Latrous, K., Doukhan, J.C., Doukhan, N., 1989. Water in diopside: an electron microscopy and infrared spectroscopy study. Eur. J. Mineral. 327–342.
Ionov, D.A., Seitz, H.M., 2008. Lithium abundances and isotopic compositions in mantle xenoliths from subduction and intra-plate settings: mantle sources vs. eruption histories. Earth Planet. Sci. Lett. 266 (3–4), 316–331.
Jugovics, L., 1971. Észak-magyarországi - Salgótarján környéki – bazaltterületek. In: Annual Report of the Geological Institute of Hugary, pp. 145–167.
Jung, H., Katayama, I., Jiang, Z., Hiraga, T., Karato, S.I., 2006. Effect of water and stress on the lattice-preferred orientation of olivine. Tectonophysics 421 (1), 1–22.
Kang, P., Lamb, W.M., Drury, M., 2017. Using mineral equilibria to estimate H_2O activities in peridotites from the Western Gneiss Region of Norway. Am. Mineral. 102 (5), 1021–1036.
Karato, S.I., Jung, H., 2003. Effects of pressure on high-temperature dislocation creep in olivine. Philos. Mag. 83 (3), 401–414.
Kázmér, M., Kovács, S., 1985. Permian-Paleogene paleogeography along the eastern part of the Insubric-Periadriatic lineament system: evidence for continental escape of the Bakony-Drauzug unit. Acta Geol. Hung. 28 (1–2), 71–84.
Kelley, S.P., Wartho, J.A., 2000. Rapid kimberlite ascent and the significance of Ar-Ar ages in xenolith phlogopites. Science 289 (5479), 609–611.
Klébesz, R., Gráczer, Z., Szanyi, Gy, Liptai, N., Kovács, I., Patkó, L., Pintér, Zs, Falus, Gy, Wesztergom, V., Szabó, Cs, 2015. Constraints on the thickness and seismic properties of the lithosphere in an extensional setting (Nógrád-Gömör Volcanic Field, Northern Pannonian Basin). Acta Geodaet. Geophys. 50 (2), 133–149.
Kohlstedt, D.L., 2006. The role of water in high-temperature rock deformation. Rev. Mineral. Geochem. 62 (1), 377–396.
Konečný, V., Lexa, J., Balogh, K., Konečný, P., 1995. Alkali basalt volcanism in Southern Slovakia: volcanic forms and time evolution. Acta Vulcanol. 7, 167–172.
Kovács, I., Szabó, C., 2008. Middle Miocene volcanism in the vicinity of the Middle Hungarian zone: evidence for an inherited enriched mantle source. J. Geodyn. 45 (1), 1–17.
Kovács, I., Zajacz, Z., Szabó, C., 2004. Type-II xenoliths and related metasomatism from the Nógrád-Gömör Volcanic Field, Carpathian-Pannonian region (northern Hungary–southern Slovakia). Tectonophysics 393 (1–4), 139–161.
Kovács, I., Hermann, J., O'Neill, H.S.C., Gerald, J.F., Sambridge, M., Horváth, G., 2008. Quantitative absorbance spectroscopy with unpolarized light: Part II. Experimental evaluation and development of a protocol for quantitative analysis of mineral IR spectra. Am. Mineral. 93 (5–6), 765–778.
Kovács, I., O'Neill, H.S.C., Hermann, J., Hauri, E.H., 2010. Site-specific infrared OH absorption coefficients for water substitution into olivine. Am. Mineral. 95 (2–3), 292–299.
Kovács, I., Falus, G., Stuart, G., Hidas, K., Szabó, C., Flower, M.F.J., Hegedűs, E., Posgay, K., Zilahi-Sebess, L., 2012a. Seismic anisotropy and deformation patterns in upper mantle xenoliths from the central Carpathian–Pannonian region: Asthenospheric flow as a driving force for Cenozoic extension and extrusion? Tectonophysics 514, 168–179.
Kovács, I., Green, D.H., Rosenthal, A., Hermann, J., O'neill, H.S.C., Hibberson, W.O., Udvardi, B., 2012b. An experimental study of water in nominally anhydrous minerals in the upper mantle near the water-saturated solidus. J. Petrol. 53 (10), 2067–2093.
Kovács, I.J., Kiss, J., Török, K., Király, E., Karátson, D., Fancsik, T., Biró, T., Pálos, Zs, Aradi, L.E., Patkó, L., Liptai, N., Falus, Gy, Hidas, K., Wesztergom, V., Szabó, Cs, 2018. A new conceptual model for the genesis of Plio-Pleistocene alkaline basalts in the Pannonian Basin. Geophys. Res. Abstr. 20 (EGU2018-9929).
Lexa, J., Seghedi, I., Németh, K., Szakács, A., Konečný, V., Pécskay, Z., Fülöp, A., Kovacs, M., 2010. Neogene-Quaternary volcanic forms in the Carpathian-Pannonian Region: a review. Cent. Eur. J. Geosci. 2 (3), 207–270.
Li, P., Xia, Q.K., Deloule, E., Chen, H., Gu, X.Y., Feng, M., 2015. Temporal variation of H_2O content in the lithospheric mantle beneath the eastern North China craton: Implications for the destruction of cratons. Gondwana Res. 28 (1), 276–287.
Libowitzky, E., Rossman, G.R., 1997. An IR absorption calibration for water in minerals. Am. Mineral. 82 (11 − 12), 1111–1115.
Liptai, N., Patkó, L., Kovács, I.J., Hidas, K., Pintér, Z., Jeffries, T., Zajacz, Z., O'Reilly, S.Y., Griffin, W.L., Pearson, N.J., Szabó, C., 2017. Multiple metasomatism beneath the Nógrád–Gömör Volcanic Field (Northern Pannonian Basin) revealed by upper mantle peridotite xenoliths. J. Petrol. 58 (6), 1107–1144.
Liptai, N., Hidas, K., Tommasi, A., Patkó, L., Kovács, I., Tommasi, A., O'Reilly, S.Y., Griffin, W.L., Pearson, N.J., Szabó, Cs, 2018. Lateral and Vertical Heterogeneity in the Lithospheric Mantle at the Margin of a Continental Extensional Basin System Reconstructed From Peridotite Xenolith Microstructures (Northern Pannonian Basin). (in prep).
Liu, X.I., O'neill, H.S.C., Berry, A.J., 2006. The effects of small amounts of H_2O, CO_2 and Na_2O on the partial melting of spinel lherzolite in the system $CaO–MgO–Al_2O_3–SiO_2 \pm H_2O \pm CO_2 \pm Na_2O$ at 1.1 GPa. J. Petrol. 47 (2), 409–434.
Liu, J., Xia, Q.K., Deloule, E., Ingrin, J., Chen, H., Feng, M., 2015. Water content and oxygen isotopic composition of alkali basalts from the Taihang Mountains, China: recycled oceanic components in the mantle source. J. Petrol. 56 (4), 681–702.
Lloyd, A.S., Ferriss, E., Ruprecht, P., Hauri, E.H., Jicha, B.R., Plank, T., 2016. An assessment of clinopyroxene as a recorder of magmatic water and magma ascent rate. J. Petrol. 57 (10), 1865–1886.
Magyar, I., Radivojević, D., Sztanó, O., Synak, R., Ujszászi, K., Pócsik, M., 2013. Progradation of the paleo-Danube shelf margin across the Pannonian Basin during the Late Miocene and Early Pliocene. Glob. Planet. Chang. 103, 168–173.
Mandler, B.E., Grove, T.L., 2016. Controls on the stability and composition of amphibole in the Earth's mantle. Contrib. Mineral. Petrol. 171 (8–9), 68.
Manthilake, M.A.G.M., Miyajima, N., Heidelbach, F., Soustelle, V., Frost, D.J., 2013. The effect of aluminum and water on the development of deformation fabrics of orthopyroxene. Contrib. Mineral. Petrol. 165 (3), 495–505.
Nimis, P., Grütter, H., 2010. Internally consistent geothermometers for garnet peridotites and pyroxenites. Contrib. Mineral. Petrol. 159 (3), 411–427.
Novák, A., Klébesz, R., Szabó, C., Wesztergom, V., Patkó, L., Liptai, N., Ádam, A., Semenov, V.Y., Lemperger, I., Kis, A., Gribovszki, K., 2014. Combined geophysical (Magnetotellurics) and Geochemical Results for Determination of the Lithosphere-Asthenosphere Boundary (LAB) Beneath the Nógrád–Gömör Volcanic Field. 22nd EM Induction Workshop, Weimar, Germany. pp. 4.
Patkó, L., Aradi, L.E., Liptai, N., Bodnar, R.J., Fedele, L., Kovács, Z., Cesare, B., Vaselli, O., Fioretti, A.M., Jeffries, T., Szabó, C., 2013. Wehrlitization processes within the upper mantle beneath the Northern Pannonian Basin (Hungary). Mineral. Mag. 77, 1934.
Pécskay, Z., Lexa, J., Szakács, A., Seghedi, I., Balogh, K., Konečný, V., Zelenka, T., Kovacs, M., Póka, T., Fülöp, A., Márton, E., Panaiotu, C., Cvetković, V., 2006. Geochronology of Neogene magmatism in the Carpathian arc and intra-Carpathian area. Geol. Carpath. Bratislava 57 (6), 511.
Peslier, A.H., 2010. A review of water contents of nominally anhydrous natural minerals in the mantles of Earth, Mars and the Moon. J. Volcanol. Geotherm. Res. 197 (1), 239–258.
Peslier, A.H., Bizimis, M., 2015. Water in Hawaiian peridotite minerals: a case for a dry metasomatized oceanic mantle lithosphere. Geochem. Geophys. Geosyst. 16 (4), 1211–1232.
Peslier, A.H., Luhr, J.F., 2006. Hydrogen loss from olivines in mantle xenoliths from Simcoe (USA) and Mexico: Mafic alkalic magma ascent rates and water budget of the sub-continental lithosphere. Earth Planet. Sci. Lett. 242 (3–4), 302–319.
Peslier, A.H., Luhr, J.F., Post, J., 2002. Low water contents in pyroxenes from spinel-peridotites of the oxidized, sub-arc mantle wedge. Earth Planet. Sci. Lett. 201 (1), 69–86.
Peslier, A.H., Schönbächler, M., Busemann, H., Karato, S.I., 2017. Water in the Earth's interior: distribution and origin. Space Sci. Rev. 212 (1–2), 743–810.
Pintér, Zs, Patkó, L., Djoukam, J.F.T., Kovács, I., Tchouankoue, J.P., Falus, Gy, Konc, Z., Tommasi, A., Barou, F., Mihály, J., Németh, Cs, Jeffries, T., 2015. Characterization of the sub-continental lithospheric mantle beneath the Cameroon volcanic line inferred from alkaline basalt hosted peridotite xenoliths from Barombi Mbo and Nyos Lakes. J. Afr. Earth Sci. 111, 170–193.
Ratschbacher, L., Frisch, W., Linzer, H.G., Merle, O., 1991. Lateral extrusion in the Eastern Alps, part 2: structural analysis. Tectonics 10 (2), 257–271.
Royden, L.H., Horváth, F., Burchfiel, B.C., 1982. Transform faulting, extension, and subduction in the Carpathian Pannonian region. Geol. Soc. Am. Bull. 93 (8), 717–725.
Sambridge, M., Gerald, J.F., Kovács, I., O'Neill, H.S.C., Hermann, J., 2008. Quantitative absorbance spectroscopy with unpolarized light: part I. Physical and mathematical development. Am. Mineral. 93 (5–6), 751–764.
Schmädicke, E., Gose, J., 2017. Water transport by subduction: clues from garnet of Erzgebirge UHP eclogite. Am. Mineral. 102 (5), 975–986.
Seghedi, I., Downes, H., Vaselli, O., Szakács, A., Balogh, K., Pécskay, Z., 2004. Post-collisional Tertiary–Quaternary mafic alkalic magmatism in the Carpathian–Pannonian region: a review. Tectonophysics 393 (1), 43–62.
Selway, K., Yi, J., Karato, S.I., 2014. Water content of the Tanzanian lithosphere from magnetotelluric data: implications for cratonic growth and stability. Earth Planet. Sci. Lett. 388, 175–186.
Sokol, A.G., Kupriyanov, I.N., Palyanov, Y.N., 2013. Partitioning of H_2O between olivine and carbonate–silicate melts at 6.3 GPa and 1400 C: Implications for kimberlite formation. Earth Planet. Sci. Lett. 383, 58–67.
Soustelle, V., Tommasi, A., Demouchy, S., Ionov, D.A., 2010. Deformation and fluid–rock interaction in the supra-subduction mantle: microstructures and water contents in peridotite xenoliths from the Avacha Volcano, Kamchatka. J. Petrol. 51 (1–2), 363–394.
Stalder, R., 2004. Influence of Fe, Cr and Al on hydrogen incorporation in orthopyroxene. Eur. J. Mineral. 16 (5), 703–711.
Stalder, R., Ludwig, T., 2007. OH incorporation in synthetic diopside. Eur. J. Mineral. 19 (3), 373–380.
Stalder, R., Skogby, H., 2002. Hydrogen incorporation in enstatite. Eur. J. Mineral. 14 (6), 1139–1144.
Stegena, L., Geczy, B., Horváth, F., 1975. Late Cenozoic evolution of the Pannonian Basin. Tectonophysics 26 (1), 71–90.
Szabó, C., Bodnar, R.J., 1996. Changing magma ascent rates in the Nógrád–Gömör volcanic field, Northern Hungary/Southern Slovakia: evidence from CO_2-rich fluid

inclusions in metasomatized upper mantle xenoliths. Petrology 4 (3), 221–230.
Szabó, C., Bodnar, R.J., 1998. Fluid-inclusion evidence for an upper-mantle origin for green clinopyroxenes in late Cenozoic basanites from the Nógrád-Gömör Volcanic Field, northern Hungary/southern Slovakia. Int. Geol. Rev. 40 (9), 765–773.
Szabó, C., Taylor, L.A., 1994. Mantle petrology and geochemistry beneath the Nógrád-Gömör volcanic field, Carpathian-Pannonian region. Int. Geol. Rev. 36 (4), 328–358.
Szabó, C., Harangi, S., Csontos, L., 1992. Review of Neogene and Quaternary volcanism of the Carpathian-Pannonian region. Tectonophysics 208 (1), 243–256.
Szabó, C., Bodnar, R.J., Sobolev, A.V., 1996. Metasomatism associated with subduction-related, volatile-rich silicate melt in the upper mantle beneath the Nógrád-Gömör volcanic field, northern Hungary/southern Slovakia; evidence from silicate melt inclusions. Eur. J. Mineral. 8 (5), 881–899.
Szafián, P., Horváth, F., Cloetingh, S., 1997. Gravity constraints on the crustal structure and slab evolution along a transcarpathian transect. Tectonophysics 272 (2–4), 233–247.
Tenner, T.J., Hirschmann, M.M., Withers, A.C., Hervig, R.L., 2009. Hydrogen partitioning between nominally anhydrous upper mantle minerals and melt between 3 and 5 GPa and applications to hydrous peridotite partial melting. Chem. Geol. 262 (1), 42–56.
Tian, Z.Z., Liu, J., Xia, Q.K., Ingrin, J., Hao, Y.T., Depecker, C., 2017. Water concentration profiles in natural mantle orthopyroxenes: a geochronometer for long annealing of xenoliths within magma. Geology 45 (1), 87–90.
Tollan, P.M., Smith, R., O'Neill, H.S.C., Hermann, J., 2017. The responses of the four main substitution mechanisms of H in olivine to H_2O activity at 1050 °C and 3 GPa. Prog. Earth Planet. Sci. 4 (1), 14.
Weiss, F.A., Ros, L., Relchart, P., Skogby, H., Kristianson, O., Dollinger, G., 2018. Hydrogen concentration analysis in clinopyroxene using proton–proton scattering analysis. Phys. Chem. Miner. 45, 669–678.
Wood, B., Bryndzia, L., Johnson, K., 1990. Mantle oxidation state and its relationship to tectonic environment and fluid speciation. Science 248 (4953), 337–345.
Xia, Q.K., Hao, Y.T., Li, P., Deloule, E., Coltorti, M., Dallai, L., Yang, X.Z., Feng, M., 2010. Low water content of the Cenozoic lithospheric mantle beneath the eastern part of the North China Craton. J. Geophys. Res. Solid Earth 115, B07207. https://doi.org/10.1029/2009 JB006694.
Xia, Q.K., Liu, J., Liu, S.C., Kovács, I., Feng, M., Dang, L., 2013a. High water content in Mesozoic primitive basalts of the North China Craton and implications on the destruction of cratonic mantle lithosphere. Earth Planet. Sci. Lett. 361, 85–97.
Xia, Q.K., Hao, Y.T., Liu, S.C., Gu, X.Y., Feng, M., 2013b. Water contents of the Cenozoic lithospheric mantle beneath the western part of the North China Craton: peridotite xenolith constraints. Gondwana Res. 23 (1), 108–118.
Xia, Q.K., Liu, J., Kovács, I., Hao, Y.T., Li, P., Yang, X.Z., Chen, H., Sheng, Y.M., 2017. Water in the Upper Mantle and Deep Crust of Eastern China: Concentration, distribution and implications. National Science Reviewhttps://doi.org/10.1093/nsr/nwx016.
Yang, X.Z., Xia, Q.K., Deloule, E., Dallai, L., Fan, Q.C., Feng, M., 2008. Water in minerals of the continental lithospheric mantle and overlying lower crust: a comparative study of peridotite and granulite xenoliths from the North China Craton. Chem. Geol. 256 (1), 33–45.
Yu, Y., Xu, X.S., Griffin, W.L., O'Reilly, S.Y., Xia, Q.K., 2011. H_2O contents and their modification in the Cenozoic subcontinental lithospheric mantle beneath the Cathaysia block, SE China. Lithos 126 (3), 182–197.
Zajacz, Z., Kovács, I., Szabó, C., Halter, W., Pettke, T., 2007. Evolution of mafic alkaline melts crystallized in the uppermost lithospheric mantle: a melt inclusion study of olivine-clinopyroxenite xenoliths, northern Hungary. J. Petrol. 48 (5), 853–883.
Zhang, H., Zheng, J., Lu, J., Pan, S., Zhao, Y., Lin, A., Xiang, L., 2018. Composition and evolution of the lithospheric mantle beneath the interior of the South China Block: insights from trace elements and water contents of peridotite xenoliths. Contrib. Mineral. Petrol. 173 (7), 53.